The Astrophysical Journal, 890:150 (21pp), 2020 February 20 https://doi.org/10.3847/1538-4357/ab6b27

A New Window into the Nature of X-Ray Binaries in M101 from Their Optical Emission

Rupali Chandar[1], Paula Johns[1], Angus Mok[1], Andrea Prestwich[2], Elena Gallo[3], and Qiana Hunt[3]
[1] Department of Physics & Astronomy, The University of Toledo, Toledo, OH 43606, USA; Rupali.Chandar@utoledo.edu
[2] Center for Astrophysics, Harvard & Smithsonian, 60 Garden Street, Cambridge, MA 02138, USA
[3] Department of Astronomy, University of Michigan, 1085 S University, Ann Arbor, MI 48109, USA
Received 2019 August 1; revised 2019 December 7; accepted 2019 December 30; published 2020 February 24

Abstract

The high-energy emission from nearby, star-forming galaxies is dominated by X-ray binaries, where a neutron star or black hole is accreting mass from either a low-mass ($\lesssim 3\ M_\odot$) or high-mass ($\gtrsim 8\ M_\odot$) star. Donor stars with intermediate masses ≈3–7 $M_\odot$ are also possible, but rarer in our Galaxy. Since it is not possible to separate low-, intermediate-, and high-mass X-ray binaries (LMXBs, IMXBs, and HMXBs) from their X-ray properties alone, we use optical images of M101 taken with the *Hubble Space Telescope* to directly constrain the masses of donor stars in X-ray binaries down to ≈3 $M_\odot$. For X-ray binaries that still live within their parent star cluster, the age of the cluster provides strong constraints on the mass of the donor and hence type of binary. We present the classification, on a source-by-source basis, of 140 X-ray point sources in the nearby spiral galaxy M101 ($D = 6.4 \pm 0.2$ Mpc). We find that, overall, HMXBs appear to follow the spiral arms, while LMXBs dominate the bulge region as expected, but also appear to form an inter-arm disk population. The X-ray luminosity functions for HMXBs and LMXBs are well fit by a power-law distribution, $dN/dL_X \propto L^\alpha$, with $\alpha = -1.71 \pm 0.06$ (HMXBs) and $\alpha = -1.96 \pm 0.08$ (LMXBs), and the brightest sources are consistent with the expectations from sampling statistics without requiring a physical cutoff. Overall, our results for HMXB and LMXB populations agree well with the specific star formation rate map presented for M101 recently by Lehmer and collaborators.

Unified Astronomy Thesaurus concepts: Spiral galaxies (1560); High mass x-ray binary stars (733); Low-mass x-ray binary stars (939); X-ray binary stars (1811)

Supporting material: machine-readable table

1. Introduction

Several studies have established that the X-ray luminosity function (XLF) of high-mass X-ray binaries (HMXBs) scales with the star formation rate (SFR) in spiral galaxies (e.g., Grimm et al. 2003; Mineo et al. 2012; hereafter Mineo+12), and that the XLF of low-mass X-ray binaries (LMXBs) scales with stellar mass in elliptical galaxies (e.g., Gilfanov 2004; Lehmer et al. 2014; Peacock & Zepf 2016). Because it is not possible to separate HMXBs from LMXBs from X-ray properties alone, most previous studies have restricted their samples to galaxies with high specific star formation rates (sSFRs; i.e., $\mathrm{SFR}/M_{*,\mathrm{host}} \gtrsim 10^{-10}$ yr^{-1}) to guarantee a significant contribution from HMXBs, or to early-type galaxies where LMXBs dominate the X-ray binary population.

The seminal work by Grimm et al. (2003) established that the XLF of HMXBs in star-forming galaxies has a near-universal shape, and that its normalization scales, at least approximately, with the global SFR of the host galaxy. These distributions can be described, to first order, by a simple power law, $dN/dL \propto L^\alpha$ with an index $\alpha \approx -1.6$. Some works have suggested that the luminosity functions may have a truncation or downturn at the upper end. This can be represented by a Schechter (1976) function, $\psi(L) \propto L^\alpha\ e^{-L/L_*}$, which is a power law with an exponential cutoff at L_*. Grimm et al. (2003) found evidence for a marginally significant break near $L_X \sim 10^{40}$ erg s^{-1}. Mineo+12 found similar results for the shape of the XLF of HMXBs when they applied a homogeneous selection and analysis to a larger sample of galaxies with $\mathrm{sSFR} \geqslant 10^{-10}$ yr^{-1}. In this work, we will distinguish between statistical and physical cutoffs in the luminosity functions. All samples have an apparent or statistical upper "cutoff" simply because they run out of objects. We are interested in establishing whether or not the data show evidence for a physical, i.e., an exponential-like, downtun at the upper end of the luminosity function that is not simply the result of sampling statistics.

As of now, our understanding of LMXB populations comes almost exclusively from elliptical and lenticular galaxies. In early-type galaxies, the number of LMXBs correlates with the total stellar mass of the galaxy (Gilfanov 2004), and approximately 25% and 70% of these LMXBs are found in ancient globular clusters (e.g., Angelini et al. 2001; Kundu et al. 2002, 2007; Sarazin et al. 2003; Jordan et al. 2004; Humphrey & Buote 2008; Peacock & Zepf 2016). The shape of the XLF for LMXBs is different from that for HMXBs, and can be described by a Schechter function with a steeper power-law index ≈−2 and a downturn at luminosities $L_X \approx$ few $\times\ 10^{38}$ erg s^{-1}.

Although it is challenging to study the XLFs of HMXBs and LMXBs in the same galaxy, Lehmer et al. (2017, 2019) recently developed a method to fit global XLFs with contributions from both types of X-ray binaries (XRBs) by estimating the star formation histories and stellar mass in ≈400 pc subregions in a sample of 38 galaxies. Contributions from X-ray background sources (CXBs) are also accounted for, and assumed to scale with the area according to the distribution presented in Kim et al. (2007). Based on their technique, Lehmer et al. (2017, 2019) found that the steepness of the XLF progresses with age, starting out shallower for the most recently formed stellar population, and becoming steeper over time, as might be expected by comparing the XLF from HMXBs in spirals with the those of LMXBs in ellipticals. Lehmer et al. (2017) also found evidence that LMXBs in ancient globular

clusters do not contribute strongly to the X-ray binary population in M51.

In this work, we develop two new techniques to classify X-ray point sources from their optical counterparts and apply them to the X-ray source population in the spiral galaxy M101. Archival images of M101 taken with the *Hubble Space Telescope* (*HST*) are deep enough to directly detect donor stars down to $M \approx 3\ M_{\odot}$, and to give reliable age estimates in the cases where XRBs still reside within their parent clusters. We assume a Cepheid-based distance of 6.4 ± 0.2 Mpc to M101 (Shappee & Stanek 2011), which gives a physical scale where $1'' \approx 31$ pc. The rest of this paper is organized as follows. Section 2 describes the catalog of X-ray point sources from *Chandra* ACIS observations of M101. Section 3 presents the optical *HST* observations, the selection of candidate donor stars and how we estimate their masses, and parent star clusters and how we estimate their ages. Here, we classify each X-ray source in M101. Section 4 presents the spatial distributions of different classes of XRBs and background sources, and Section 5 presents their luminosity functions. In Section 6 we discuss the implications of our findings for HMXB, LMXBs, and background galaxies, and summarize our main results in Section 7.

2. Catalog and X-Ray Source Classification

2.1. Catalog of X-Ray Point Sources in M101

M101 has been extensively observed by the ACIS instrument on *Chandra*, with 27 individual exposures totalling close to 1 Ms. The *Chandra* X-ray Center recently released their second source catalog for observations taken through the end of 2014 (see Evans et al. 2010), providing a homogeneous catalog of thousands of X-ray sources in tens of nearby late-type galaxies. The second release source catalog is thus an excellent starting point for this project, and includes a number of improvements over the first release. The source catalog stacks together all observations of the same area of sky that are centered within 1 arcmin, increasing the depth of the catalog. Detections from different stacks are cross-matched to derive the unique CSC 2.0 source list. Some other improvements include:

1. two-step source detection;
2. point-spread function (PSF) modeling;
3. exclusion of extended sources.

All of the data are processed in a uniform way through the standard CIAO pipeline, and output fluxes measured in three different energy bands: soft or "S" (0.3–1.5 keV), medium or "M" (1.5–2.5 keV), and hard or "H" (2.5–8 keV). These are converted to luminosities by assuming a distance of 6.4 ± 0.2 Mpc to M101.

We selected an initial X-ray list by searching for sources observed with the ACIS detector within $6'$ of the center of M101, using the following criteria:

1. significance >3.0;
2. extent_flag = false;
3. sat_source_flag = false;
4. streak_source_flag = false.

These flags are intended to remove extended sources, those that are saturated in all observations, and spurious detections located on an ACIS readout streak in all observations.

We find that 140 X-ray sources fall within the $\approx 10' \times 10'$ optical mosaic of M101 described in the next section. Table 1 compiles the R.A., decl., and total X-ray flux (from the S+M +H bands) for each of these X-ray sources.

Because different regions within M101 have been imaged to different depths, it is not straightforward to determine the flux (luminosity) limit of our sample directly from the observations. Instead, we use the XLF itself to estimate this limit. In Section 5 we find that, as expected, the shape of the XLF is well described to first order by a power law over most of the plotted range, but flattens at lower luminosities. We assume that this flattening is the result of incompleteness and, based on its location, we adopt a completeness limit of $L_X = 3 \times 10^{36}$ erg s^{-1}.

2.2. HST Observations and Alignment

M101 has been observed with the *HST* through several different programs. Here, we use the 10 pointings observed in the *B*, *V*, and *I* bands with the Wide Field Channel (WFC) of the Advanced Camera for Surveys (ACS) taken as part of program GO-9490 (PI: K. Kuntz). Each pointing was observed with two exposures for a total of 15 minutes in the *B* band, and 12 minutes in each of the *V* and *I* bands. No dithering was performed. We show a *V*-band mosaic of the 10 fields in Figure 1. The mosaic covers an area of 106 square arcminutes, extending out $\approx 10'$ from the center of M101. The white lines are the gaps between the two detectors that make up the ACS/WFC, where no data are available.

We use the following procedure to align the *Chandra* X-ray source coordinates and the optical *HST* mosaic. We compared the positions of 13 background galaxies and foreground stars (X11, X39, X55, X66, X80, X101, X113, X116, X114, X171, X166, X177, and X180) that can be well-centered in the *HST* mosaic, found that the positions of the optical counterparts are shifted by $0\farcs6$, and applied a shift to the *HST* coordinates to align them to the X-ray positions. We find that the random errors are fairly small, $\approx 0\farcs3$, from the standard deviation of the separations between the X-ray and optical coordinates for these 13 sources after shifting. Our estimate of the astrometric uncertainty in the X-ray coordinates in M101 is similar to that found previously for the Antennae by Rangelov et al. (2012).

In Figure 2, we show postage stamps, a $1\farcs7 \times 1\farcs7$ portion of the optical *BVI* color image centered at the location of each X-ray source. Positional uncertainties of $1\sigma = 0\farcs3$ and $2\sigma = 0\farcs6$ are shown as the two centered circles. Potential donor stars or parent clusters are shown as the smaller circles. We find that the thumbnails can be broadly characterized in one of three ways. Some X-ray sources do not have any obvious optical counterpart detected within the 2σ positional uncertainty (e.g., X1, X3, and X5). When there is no detected optical counterpart, it is very likely that there is a low-mass donor that is below the detection limit, and hence the source is a likely to be an LMXB. In other cases, a clear, dominant single source is detected within 2σ (e.g., X18, X22, and X32), while the rest have multiple optical sources within 2σ (e.g., X7, X12, and 24).

For the sources where optical counterparts are detected within 2σ, we use their properties to classify each X-ray source as: a foreground star, donor star in M101 (XRB, either HMXB or IMXB), compact star cluster host (XRB, discussed further in Section 3.2), or a quasar or AGN in a background galaxy. Foreground dwarf stars are red and quite bright. AGNs are relatively easy to identify, because the surrounding host galaxy is fairly obvious in *HST* images. Typically, when there are multiple potential optical counterparts, it is because the X-ray

Table 1
M101 X-Ray Point Source Properties

XID	R.A. (J2000)	Decl. (J2000)	$\log(L_x)$ ($\times 10^{36}$ erg s^{-1})	V (mag)	$B-V$ (mag)	$V-I$ (mag)	Classification	QF	Notes
1	210.80459478	54.34798659	0.33 ± 1.23	⋯	⋯	⋯	LMXB	1	
2	210.81203354	54.35288294	6.93 ± 12.44	21.40 ± 0.02	0.76 ± 0.07	1.14 ± 0.04	LMXB	1	Old globular cluster
3	210.78921548	54.34797275	2.83 ± 3.37	⋯	⋯	⋯	LMXB	2	
4	210.79067377	54.35415710	16.58 ± 15.05	⋯	⋯	⋯	Foreground star	1	
5	210.81177559	54.35640599	3.46 ± 6.36	⋯	⋯	⋯	LMXB	1	
7	210.79470128	54.35730647	3.18 ± 5.05	23.79 ± 0.07	−0.14 ± 0.17	−0.18 ± 0.24	Intermediate-mass X-ray binary (IMXB)	3	
8	210.81871469	54.35156777	10.55 ± 10.70	⋯	⋯	⋯	LMXB	1	
9	210.80807936	54.36014507	4.87 ± 7.18	⋯	⋯	⋯	LMXB	1	
10	210.81296842	54.33833502	4.43 ± 5.25	⋯	⋯	⋯	LMXB	1	
11	210.80680496	54.33595766	8.95 ± 7.20	25.67 ± 0.12	0.58 ± 0.35	0.14 ± 0.30	IMXB	1	
12	210.78339349	54.35642577	2.16 ± 2.26	23.20 ± 0.03	0.02 ± 0.08	0.17 ± 0.09	HMXB	2	
13	210.80707693	54.36301871	23.81 ± 13.83	⋯	⋯	⋯	LMXB	1	
14	210.81095628	54.36444162	1.18 ± 2.16	⋯	⋯	⋯	LMXB	1	
15	210.80544153	54.36585707	5.12 ± 10.20	⋯	⋯	⋯	LMXB	1	
16	210.77579911	54.33658448	14.17 ± 17.41	26.67 ± 0.15	⋯	2.29 ± 0.22	IMXB	1	
18	210.83026118	54.36368372	13.58 ± 8.02	⋯	⋯	⋯	Foreground star	1	
19	210.82291324	54.36843285	12.10 ± 13.25	⋯	⋯	⋯	LMXB	1	
20	210.77915586	54.36927218	13.48 ± 11.50	26.04 ± 0.13	0.36 ± 0.39	0.41 ± 0.36	HMXB	1	
21	210.84444158	54.34407150	2.64 ± 4.24	22.94 ± 0.04	0.44 ± 0.13	1.01 ± 0.08	IMXB	3	few 100 Myr cluster
22	210.78086832	54.32721238	109.31 ± 40.34	24.60 ± 0.06	0.69 ± 0.19	1.04 ± 0.11	HMXB	1	
23	210.76094602	54.35570284	8.63 ± 15.18	⋯	⋯	⋯	LMXB	1	
24	210.77502722	54.32913878	10.03 ± 8.78	23.45 ± 0.04	−0.05 ± 0.10	−0.04 ± 0.12	HMXB	2	
25	210.75549539	54.35924087	3.70 ± 6.57	24.81 ± 0.10	0.87 ± 0.37	1.71 ± 0.14	HMXB	2	
26	210.77750088	54.37454735	14.63 ± 15.14	25.58 ± 0.14	0.43 ± 0.40	2.36 ± 0.19	Active galactic nucleus (AGN)	1	
27	210.80711419	54.31912856	15.95 ± 7.54	⋯	⋯	⋯	LMXB	1	
28	210.75331483	54.33813272	1.44 ± 2.59	⋯	⋯	⋯	LMXB	1	
29	210.85490106	54.34717202	16.00 ± 9.42	⋯	⋯	⋯	LMXB	1	
30	210.76975287	54.32349042	0.22 ± 0.87	20.29 ± 0.01	0.15 ± 0.03	0.38 ± 0.02	HMXB	2	
31	210.75599698	54.36568047	0.17 ± 0.69	26.51 ± 0.14	1.91 ± 0.84	1.66 ± 0.24	IMXB	1	
32	210.74769287	54.34518583	5.01 ± 9.63	26.39 ± 0.13	−0.63 ± 0.31	1.04 ± 0.34	IMXB	1	
33	210.75209971	54.33396490	2.25 ± 3.72	24.74 ± 0.07	−0.07 ± 0.17	0.29 ± 0.21	IMXB	1	
34	210.85553408	54.33771635	17.36 ± 14.92	26.08 ± 0.14	0.60 ± 0.45	1.34 ± 0.25	IMXB	1	
35	210.85768551	54.35690851	1.00 ± 2.25	25.03 ± 0.10	0.29 ± 0.26	0.91 ± 0.23	HMXB	1	On 8 $M_\odot$ line
36	210.86109840	54.34518277	5.53 ± 7.79	25.84 ± 0.12	0.22 ± 0.37	0.65 ± 0.31	IMXB	3	Cluster
37	210.78774492	54.38302663	11.92 ± 11.98	25.73 ± 0.13	1.06 ± 0.59	2.12 ± 0.19	IMXB	1	Extended in I
38	210.83816797	54.31888386	9.07 ± 19.89	⋯	⋯	⋯	LMXB	2	

Table 1
(Continued)

XID	R.A. (J2000)	Decl. (J2000)	$\log(L_x)$ ($\times 10^{36}$ erg s^{-1})	V (mag)	$B-V$ (mag)	$V-I$ (mag)	Classification	QF	Notes
39	210.85909281	54.33075178	6.21 ± 14.34	22.36 ± 0.02	−0.06 ± 0.05	0.01 ± 0.06	HMXB	2	
40	210.84008322	54.37935524	6.60 ± 12.35	⋯	⋯	⋯	LMXB	1	
41	210.87024789	54.34968002	2.63 ± 5.74	⋯	⋯	⋯	LMXB	1	
42	210.86986355	54.35357395	3.24 ± 4.77	21.56 ± 0.02	0.19 ± 0.04	0.33 ± 0.04	HMXB	1	Blended with faint star
43	210.86625431	54.33456839	5.08 ± 7.52	23.98 ± 0.06	0.35 ± 0.20	1.02 ± 0.13	IMXB	1	Few 100 Myr cluster
44	210.78278101	54.31014354	17.04 ± 12.52	25.03 ± 0.08	0.81 ± 0.27	1.11 ± 0.16	HMXB	1	
45	210.81980715	54.30967130	6.71 ± 8.09	⋯	⋯	⋯	LMXB	2	
46	210.82389077	54.30995830	49.48 ± 19.08	25.72 ± 0.13	−0.05 ± 0.35	1.22 ± 0.28	HMXB	2	
47	210.86117856	54.37245444	3.89 ± 6.99	⋯	⋯	⋯	LMXB	1	
48	210.77202725	54.38653937	4.32 ± 5.61	27.75 ± 0.16	0.46 ± 0.93	3.67 ± 0.21	IMXB	1	
49	210.73182869	54.34130163	9.27 ± 30.23	23.67 ± 0.05	−0.10 ± 0.11	0.03 ± 0.14	HMXB	1	
50	210.87467999	54.34931157	3.31 ± 5.37	25.51 ± 0.10	0.07 ± 0.26	0.02 ± 0.37	IMXB	1	
51	210.87078105	54.36364921	1.70 ± 3.72	26.22 ± 0.14	−0.13 ± 0.38	−2.33 ± 0.55	HMXB	1	
52	210.86926347	54.36719895	3.01 ± 7.96	⋯	⋯	⋯	LMXB	1	
53	210.73475045	54.32977803	4.49 ± 6.60	25.70 ± 0.11	0.18 ± 0.27	0.48 ± 0.27	IMXB	1	
54	210.81683350	54.30540505	13.82 ± 13.36	24.26 ± 0.08	0.39 ± 0.23	0.53 ± 0.19	IMXB	3	Few 100 Myr cluster
55	210.81385375	54.39361678	6.03 ± 12.55	⋯	⋯	⋯	HMXB	1	Supergiant. No V-band photometry
56	210.78601281	54.39344450	0.69 ± 1.45	23.97 ± 0.05	−0.18 ± 0.11	−0.28 ± 0.15	HMXB	2	
57	210.80821596	54.30282152	18.73 ± 44.32	⋯	⋯	⋯	LMXB	2	
58	210.78487416	54.30319033	17.75 ± 16.39	25.38 ± 0.11	0.76 ± 0.44	2.41 ± 0.15	AGN	1	
59	210.80961551	54.30171040	205.97 ± 540.62	23.26 ± 0.04	−0.04 ± 0.10	0.17 ± 0.11	HMXB	1	
60	210.75875767	54.39023855	1.56 ± 3.24	24.35 ± 0.06	0.31 ± 0.18	0.51 ± 0.16	HMXB	2	
61	210.87486082	54.37464663	20.47 ± 32.79	22.91 ± 0.04	0.07 ± 0.10	−0.24 ± 0.12	HMXB	2	
62	210.84573878	54.30612660	1.09 ± 2.56	24.69 ± 0.08	0.25 ± 0.23	0.91 ± 0.19	IMXB	1	Few 100 Myr cluster
63	210.80269914	54.29896462	1.02 ± 2.05	22.69 ± 0.03	−0.17 ± 0.07	−0.26 ± 0.09	HMXB	2	
64	210.72877795	54.37429839	7.74 ± 20.56	23.08 ± 0.03	−0.13 ± 0.07	−0.19 ± 0.10	HMXB	2	
65	210.87806505	54.37267451	42.67 ± 19.08	⋯	⋯	⋯	LMXB	1	
66	210.80193387	54.29825264	14.14 ± 7.20	22.80 ± 0.03	0.11 ± 0.08	0.26 ± 0.09	HMXB	2	
67	210.71509138	54.34796645	2.33 ± 4.17	25.68 ± 0.11	0.84 ± 0.42	2.12 ± 0.16	IMXB	1	
68	210.86581629	54.31305996	5.19 ± 10.02	23.86 ± 0.05	−0.11 ± 0.13	0.08 ± 0.15	HMXB	1	
69	210.79379239	54.29703434	6.29 ± 5.96	⋯	⋯	⋯	LMXB	1	
70	210.71280908	54.34491676	2.00 ± 4.18	24.21 ± 0.05	0.11 ± 0.14	−0.06 ± 0.17	HMXB	1	
71	210.85014185	54.39360325	6.37 ± 8.64	24.02 ± 0.06	−0.11 ± 0.13	−0.28 ± 0.18	HMXB	1	
72	210.86323647	54.30868588	19.90 ± 13.84	21.06 ± 0.01	1.16 ± 0.05	1.05 ± 0.03	HMXB	1	Red supergiant
73	210.73980026	54.30943856	7.73 ± 10.74	24.68 ± 0.07	−0.33 ± 0.15	−0.24 ± 0.21	HMXB	1	

Table 1
(Continued)

XID	R.A. (J2000)	Decl. (J2000)	$\log(L_x)$ ($\times 10^{36}$ erg s^{-1})	V (mag)	$B-V$ (mag)	$V-I$ (mag)	Classification	QF	Notes
74	210.75486796	54.39484672	6.12 ± 8.73	23.90 ± 0.05	0.14 ± 0.13	0.27 ± 0.13	HMXB	1	
75	210.88708755	54.37043242	0.87 ± 3.67	24.84 ± 0.10	−0.28 ± 0.20	0.01 ± 0.26	HMXB	2	Frame cutoff
76	210.77176774	54.29781155	35.67 ± 23.68	23.30 ± 0.04	0.36 ± 0.10	1.12 ± 0.08	HMXB	1	
77	210.87770210	54.38045196	4.35 ± 7.96	25.52 ± 0.13	0.05 ± 0.28	0.36 ± 0.33	IMXB	1	
78	210.72580554	54.31723309	19.34 ± 21.48	⋯	⋯	⋯	LMXB	2	
79	210.71582026	54.32569266	3.72 ± 9.80	⋯	⋯	⋯	LMXB	2	
80	210.89711735	54.35657179	8.30 ± 12.33	26.76 ± 0.22	1.14 ± 0.87	2.54 ± 0.31	AGN	1	Extended in I
81	210.85526954	54.39523338	20.40 ± 18.91	⋯	⋯	⋯	LMXB	2	
82	210.80222983	54.40499822	14.68 ± 10.45	⋯	⋯	⋯	LMXB	1	
83	210.72226410	54.31554729	2.16 ± 3.19	⋯	⋯	⋯	AGN	1	
84	210.70688228	54.33323370	6.54 ± 6.70	⋯	⋯	⋯	LMXB	1	
85	210.71410311	54.37542647	2.39 ± 5.35	⋯	⋯	⋯	LMXB	1	
86	210.71369316	54.32171265	5.47 ± 10.76	25.59 ± 0.12	−0.01 ± 0.31	0.36 ± 0.33	IMXB	1	Two blended stars
87	210.79642295	54.29039124	3.22 ± 6.02	⋯	⋯	⋯	LMXB	2	
88	210.87038673	54.39228904	0.72 ± 3.01	⋯	⋯	⋯	LMXB	2	
89	210.76405312	54.29357106	4.99 ± 6.68	⋯	⋯	⋯	LMXB	2	
90	210.70108101	54.34093576	4.21 ± 6.43	⋯	⋯	⋯	LMXB	1	
91	210.89962087	54.36738890	2.56 ± 6.64	⋯	⋯	⋯	AGN	1	
92	210.73032979	54.39161623	1.69 ± 4.39	⋯	⋯	⋯	LMXB	2	
93	210.82776933	54.40821670	54.51 ± 21.08	24.73 ± 0.06	0.81 ± 0.24	1.97 ± 0.10	HMXB	1	Red supergiant
95	210.73913038	54.29963523	6.37 ± 12.44	25.12 ± 0.10	3.04 ± 1.29	2.86 ± 0.13	AGN	3	
96	210.90759382	54.34406218	6.19 ± 11.43	26.41 ± 0.21	0.29 ± 0.56	1.23 ± 0.42	IMXB	3	Few 100 Myr cluster
97	210.82925794	54.28876685	3.21 ± 12.23	⋯	⋯	⋯	LMXB	2	
98	210.90012735	54.32354306	147.91 ± 70.70	25.02 ± 0.08	−0.18 ± 0.20	−0.15 ± 0.23	HMXB	1	
99	210.88962959	54.38531463	8.19 ± 16.13	⋯	⋯	⋯	LMXB	2	Red source only in I band
100	210.73913207	54.29801390	4.01 ± 6.03	23.05 ± 0.03	−0.14 ± 0.08	−0.04 ± 0.10	HMXB	1	
101	210.77981649	54.41015113	0.51 ± 1.46	⋯	⋯	⋯	LMXB	1	
102	210.86553267	54.40002228	18.08 ± 15.57	⋯	⋯	⋯	AGN	1	
104	210.81864085	54.28550109	1.36 ± 3.59	24.58 ± 0.07	−0.20 ± 0.17	−0.11 ± 0.21	HMXB	1	
105	210.81456628	54.28443102	9.33 ± 13.13	22.36 ± 0.03	0.80 ± 0.13	−0.51 ± 0.13	HMXB	2	Young 3–5 Myr cluster
106	210.71001488	54.38507362	13.29 ± 13.93	⋯	⋯	⋯	LMXB	2	
108	210.74914880	54.40709003	3.00 ± 6.37	⋯	⋯	⋯	LMXB	2	
109	210.70463775	54.31164367	10.23 ± 8.25	20.50 ± 0.01	0.06 ± 0.03	0.59 ± 0.03	IMXB	3	Few tens of Myr compact cluster
110	210.83945839	54.28409742	7.10 ± 13.11	25.02 ± 0.08	−0.12 ± 0.20	0.27 ± 0.24	IMXB	3	
111	210.86833875	54.40512702	0.69 ± 3.06	26.67 ± 0.15	−0.68 ± 0.34	−0.45 ± 0.46	IMXB	1	
112	210.78502515	54.41639559	51.04 ± 31.02	⋯	⋯	⋯	Foreground star	1	

Table 1
(Continued)

XID	R.A. (J2000)	Decl. (J2000)	$\log(L_x)$ ($\times 10^{36}$ erg s^{-1})	V (mag)	$B-V$ (mag)	$V-I$ (mag)	Classification	QF	Notes
113	210.70296924	54.38642848	4.16 ± 7.96	⋯	⋯	⋯	LMXB	2	
114	210.68400126	54.34297283	3.19 ± 6.62	25.88 ± 0.11	−0.53 ± 0.23	1.06 ± 0.27	IMXB	3	
115	210.87895321	54.29539378	0.10 ± 0.35	23.53 ± 0.04	0.21 ± 0.11	1.11 ± 0.07	HMXB	2	
116	210.88890563	54.29992144	11.23 ± 15.24	26.16 ± 0.14	−0.33 ± 0.31	0.80 ± 0.41	IMXB	3	
117	210.68270016	54.33491545	6.87 ± 10.00	24.74 ± 0.10 24.23 ± 0.06 25.45 ± 0.11	−0.21 ± 0.21 −0.06 ± 0.15 −0.18 ± 0.25	0.12 ± 0.28 −0.25 ± 0.19 −0.01 ± 0.29	HMXB	3	Multiple potential donors
118	210.70125190	54.30798340	5.96 ± 7.98	25.43 ± 0.09	0.31 ± 0.28	0.58 ± 0.21	IMXB	1	
119	210.90106592	54.30408902	64.34 ± 17.99	⋯	⋯	⋯	AGN	1	Elliptical galaxy
120	210.88443088	54.40386885	2.71 ± 7.09	24.86 ± 0.07	0.64 ± 0.21	0.89 ± 0.14	HMXB	1	
121	210.71414651	54.29676623	20.94 ± 14.13	25.31 ± 0.10	−0.02 ± 0.23	0.37 ± 0.25	IMXB	3	
122	210.67816566	54.33781145	4.55 ± 8.22	25.35 ± 0.11	0.55 ± 0.29	0.89 ± 0.23	IMXB	1	
123	210.86123572	54.28215899	7.98 ± 16.34	26.94 ± 0.17	0.19 ± 0.43	0.19 ± 0.37	IMXB	1	
124	210.83543333	54.27565217	54.30 ± 9.85	24.95 ± 0.08	−0.06 ± 0.21	−0.52 ± 0.28	Quasar Candidate	3	Red source only in I-band
125	210.89894820	54.40025523	3.80 ± 3.01	25.25 ± 0.09	0.23 ± 0.23	1.16 ± 0.17	HMXB	2	
126	210.77128173	54.42285314	4.90 ± 6.32	25.82 ± 0.13	⋯	2.81 ± 0.15	HMXB	1	Red supergiant
127	210.91389098	54.30764096	18.17 ± 14.07	⋯	⋯	⋯	AGN	1	
128	210.92470390	54.31924715	2.26 ± 3.86	26.66 ± 0.14	2.36 ± 0.84	1.74 ± 0.25	IMXB	3	
129	210.79072505	54.27101538	6.54 ± 11.15	24.61 ± 0.07	0.08 ± 0.19	0.13 ± 0.22	HMXB	1	Blended stars
132	210.94204046	54.36599325	0.59 ± 1.35	⋯	⋯	⋯	LMXB	2	Red source only in I-band
134	210.89811721	54.28573529	130.52 ± 71.12	⋯	⋯	⋯	Foreground star	1	
140	210.95110139	54.35478793	2.38 ± 3.83	⋯	⋯	⋯	LMXB	1	
141	210.81724163	54.43568296	13.71 ± 23.70	⋯	⋯	⋯	LMXB	1	
143	210.94745104	54.37488239	13.01 ± 13.12	⋯	⋯	⋯	Foreground Star	1	
145	210.76982219	54.25950349	12.94 ± 18.14	⋯	⋯	⋯	LMXB	2	
146	210.91189135	54.28195928	21.36 ± 16.10	26.97 ± 0.20	1.56 ± 0.87	1.44 ± 0.35	IMXB	1	
149	210.95392701	54.37852061	1.73 ± 3.02	26.88 ± 0.30	0.77 ± 1.01	2.08 ± 0.37	IMXB	1	Hot pixel visible
150	210.93653091	54.40040714	47.06 ± 21.23	25.01 ± 0.09	0.83 ± 0.29	1.85 ± 0.13	HMXB	1	Hot pixel visible
151	210.96371322	54.34743304	13.61 ± 14.39	23.08 ± 0.03	0.11 ± 0.08	0.21 ± 0.08	HMXB	1	
155	210.66204185	54.29893782	26.31 ± 24.86	25.39 ± 0.12	0.27 ± 0.37	0.75 ± 0.27	IMXB	3	
156	210.96636761	54.36376970	14.33 ± 20.83	22.84 ± 0.04 24.22 ± 0.08 23.35 ± 0.05 24.89 ± 0.11	0.10 ± 0.08 1.10 ± 0.39 −0.19 ± 0.09 −0.33 ± 0.19	−0.30 ± 0.10 1.79 ± 0.11 0.17 ± 0.11 −0.10 ± 0.24	HMXB	2	Multiple potential donors
158	210.90295808	54.27075074	4.15 ± 7.39	⋯	⋯	⋯	LMXB	1	
160	210.63546753	54.33369052	109.95 ± 49.16	⋯	⋯	⋯	Foreground star	1	
161	210.94461876	54.40242372	3.37 ± 6.76	⋯	⋯	⋯	LMXB	1	
162	210.96941626	54.36976485	1.77 ± 3.08	29.15 ± 0.45	⋯	5.79 ± 0.46	HMXB	1	

(This table is available in machine-readable form.)

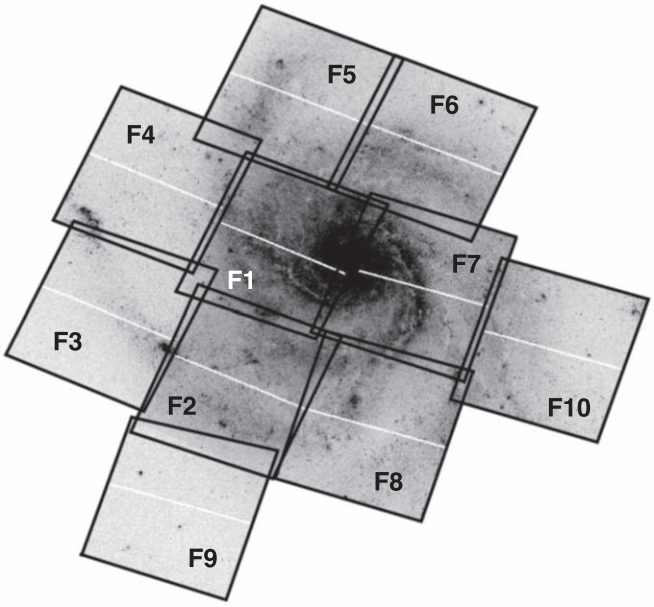

Figure 1. *V*-band mosaic of the 10 *HST* fields in M101 used in this work.

source is in a region of active star formation, where there are lots of young massive stars, making the source likely to be an HMXB. Star clusters are broader than the PSF, and are distinguished from an individual or close pair of stars from their radial profiles (see the description in Chandar et al. 2010, for example). The remaining counterparts are the donor stars in the X-ray binary.

3. Classification of X-Ray Sources

In this section, we describe and apply the methods used to classify each X-ray source in the CSC catalog of M101, based on its optical properties.

3.1. Classification Based on Donor Star Mass

For each X-ray source, we identify all optical sources located within 2σ, and perform aperture photometry to estimate their luminosities in each filter (see the technical description in, e.g., Chandar et al. 2010). We perform aperture photometry on each detected optical source that (has a center that) lies within the 2σ circle, using a three-pixel aperture. We correct for missing flux by using the encircled energy distribution tables for point sources given in Sirianni et al. (2005), and convert to the VEGAMAG system by using the zero-point for each filter that is given on the ACS instrument page. We record the V magnitude and the $V-I$ color for each source in Table 2 (a number of sources are not detected in the B band, since it does not go as deep).

We find that we can detect optical sources down to $m_V \approx 28$ mag, which is deep enough to detect a $\approx 3\ M_\odot$ star at the distance of M101. This is a critical point: *if we cannot detect a donor star directly in the optical image, then the source is very likely to be an LMXB.* We have checked the *HST* observations of M101, and this is true throughout the images, except in a few small portions in the most crowded part of the spiral arm and nuclear regions. In M101, we find that no donor star is detected within $0\farcs6$ of the location of 47 X-ray sources from the point-source catalog.

For each potential donor star, we compare the measured colors and magnitudes with theoretical isochrones from the Padova models (Bertelli et al. 1994; Girardi et al. 2008; Marigo et al. 2008) at solar metallicity. We correct the donor star photometry for foreground extinction, which is quite low toward M101, with $A_V \approx 0.02$ mag and $E(V-I) \approx 0.01$ mag. This comparison is shown in Figure 3, along with the evolutionary tracks for 3, 5, 8, 20, and 40 $M_\odot$ stars from the PARSEC models (e.g., Marigo et al. 2008). Solar metallicity is appropriate for the radii covered by our study, since the well-known metallicity drop in M101 occurs a little further out.

Figure 3 shows several interesting results. First, the lowest-luminosity donor stars that we detect reach down to $\approx 3\ M_\odot$, and the masses extend from there up to $\approx 40\ M_\odot$. Approximately one-third of detected donor stars have masses higher than $\gtrsim 8\ M_\odot$, and a number have estimated masses between 3 and 7 $M_\odot$. If the extinction for these stars is less than $A_V \approx$ 1–2 mag, then they are candidate intermediate-mass donors; if the extinction is higher than this, they will have estimated masses $\gtrsim 8\ M_\odot$. To get a handle on the extinction that may be affecting the photometry of our donor stars, we examine the *BVI* color images of each potential intermediate-mass donor, and find that there is very little visual evidence for dust lanes or dark patches that might cause extinction (with the exception of X11, X34, X110, X111, X122, X123, and X128), and which show up nicely in other parts of the mosaic.

The classification for each source is given in Table 1. When no optical source is detected within $2\sigma = 0\farcs6$, the source is classified as an LMXB. Most of these sources appear to be in regions of M101 with low background and extinction. Sources with a donor star within 2σ that has a mass consistent with the 8 $M_\odot$ or higher isochrone are classified as an HMXB. Note that there are a number of XRBs in crowded regions, where it is not possible to tell exactly which star is the donor. In most of these cases, *all* potential donor stars have estimated masses of 8 $M_\odot$ or higher, and the source is classified as an HMXB.

We also assign each X-ray source a "confidence" flag, where 1 = high confidence, 2 = medium confidence, and 3 = low confidence (Table 1). X-ray sources with one candidate donor within 2σ in a region of low extinction will be assigned a Flag = 1. LMXBs with a high background are given lower confidences (Flag = 2) since there is a possibility of an intermediate-mass star going undetected. Similarly, IMXBs detected in regions with high backgrounds are given lower confidences (Flag = 2) since the photometry is less certain. LMXBs are given a low confidence (Flag = 3) if a dim optical source is detected exactly 2σ from the X-ray source. HMXBs and IMXBs are given low confidences (Flag = 3) if there are multiple optical sources within 2σ so we cannot uniquely identify the donor, and the potential donors have very different mass estimates. HMXBs and IMXBs are assigned a Flag = 2 if there are multiple optical sources within 2σ so we cannot uniquely identify the donor, yet all optical sources fall within the same mass range. If the X-ray source is located within the nucleus of the galaxy, we assign the classification a low confidence (Flag = 3).

In this work, we do not make any explicit correction to the photometry of donor stars for extinction. If we had, it is possible that the luminosity of a few "intermediate-mass" 3–7 $M_\odot$ stars would increase enough to push them above 8 $M_\odot$, i.e., into the regime of HMXBs. From the optical images we assess, on a case-by-case basis, the level of extinction that we think may be affecting the source, due to the presence of

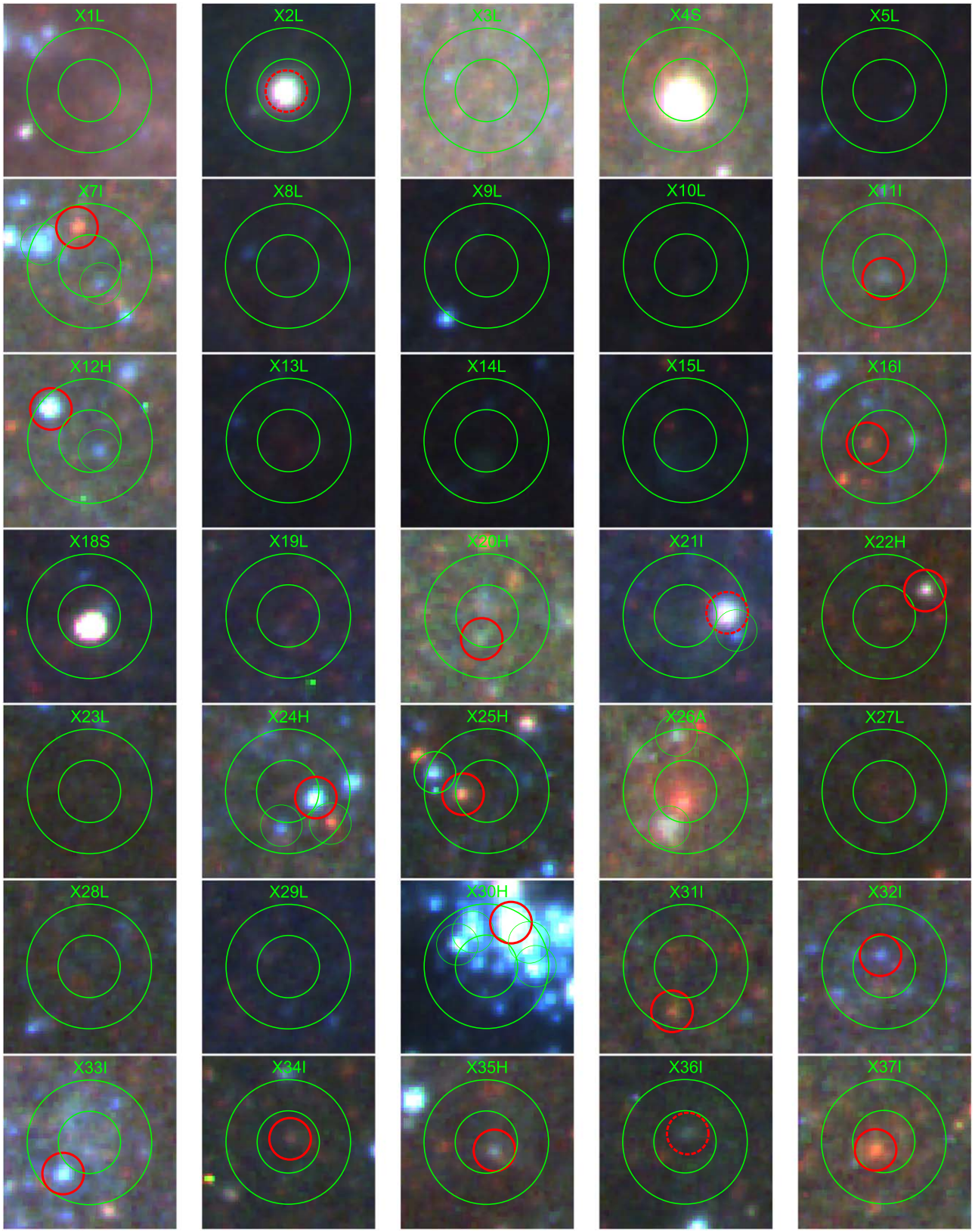

Figure 2. A $1.7 \times 1\farcs7$ portion of an optical color image (*BVI*) centered at the position of the labeled X-ray source detection. The two green concentric circles represent $1\sigma = 0\farcs3$ and $2\sigma = 0\farcs6$ positional uncertainties, which were determined as described in the text. The smaller green circles show the locations of detected sources within 2σ, and the red circles show the most likely donor. The classification of each source is given after its identification: "H" = high-mass XRB, "I" = intermediate-mass XRB, "L" = low-mass XRB, "A" = AGN/quasar, "S" = foreground star.

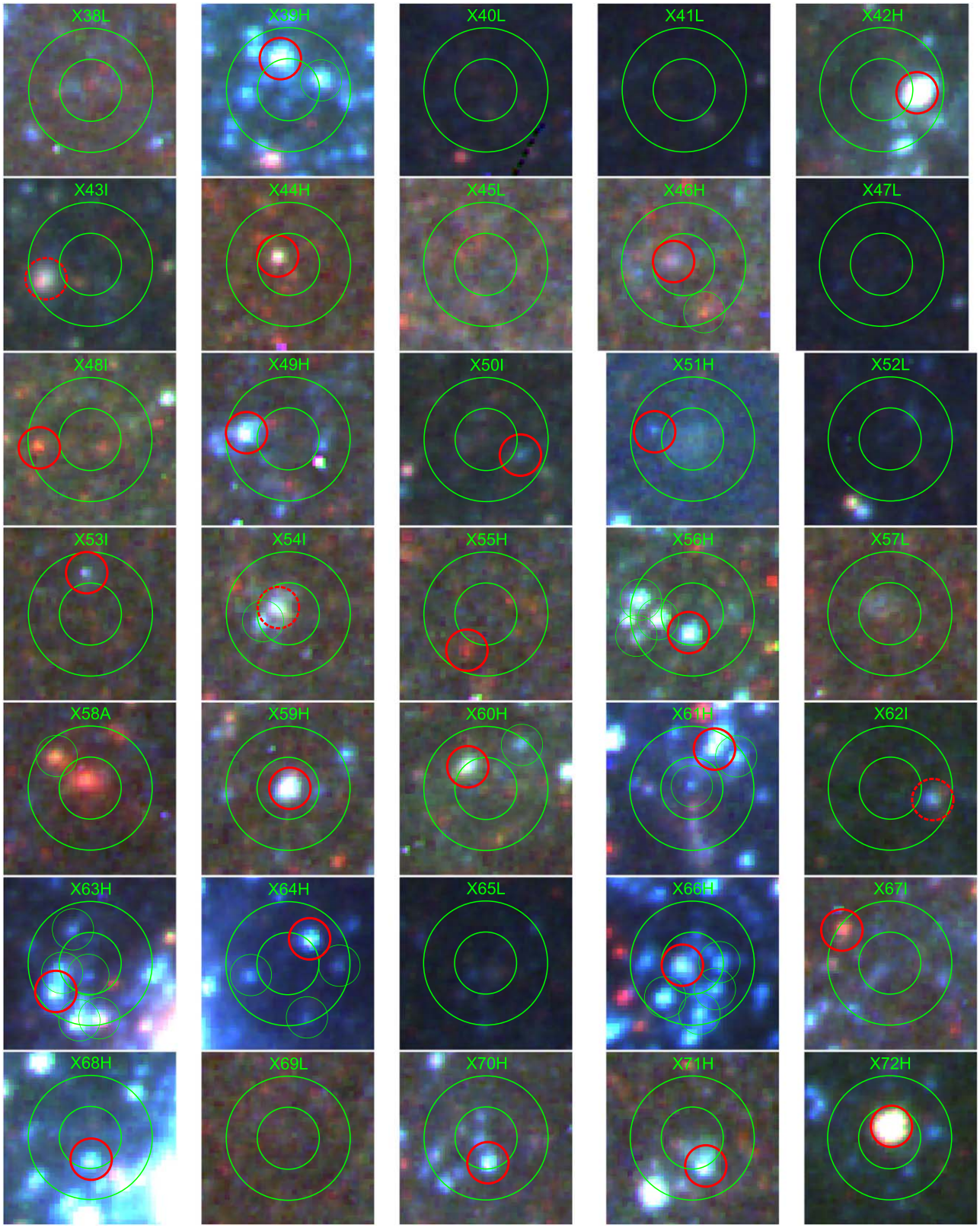

Figure 2. (Continued.)

dark patches and dust lanes. For the vast majority of our sources, we do not see visual evidence of extinction, suggesting that A_V is quite low.

Thus far, we have assumed a simplistic model for the uncertainty associated with the X-ray source positions, one that can be represented by a circle with a 1σ radius of $0\farcs3$. However, sources that are not close to a central pointing position will have degraded and non-symmetric errors. We assess the impact that larger positional uncertainties might have on our results by examining a $1''$ radius region around each

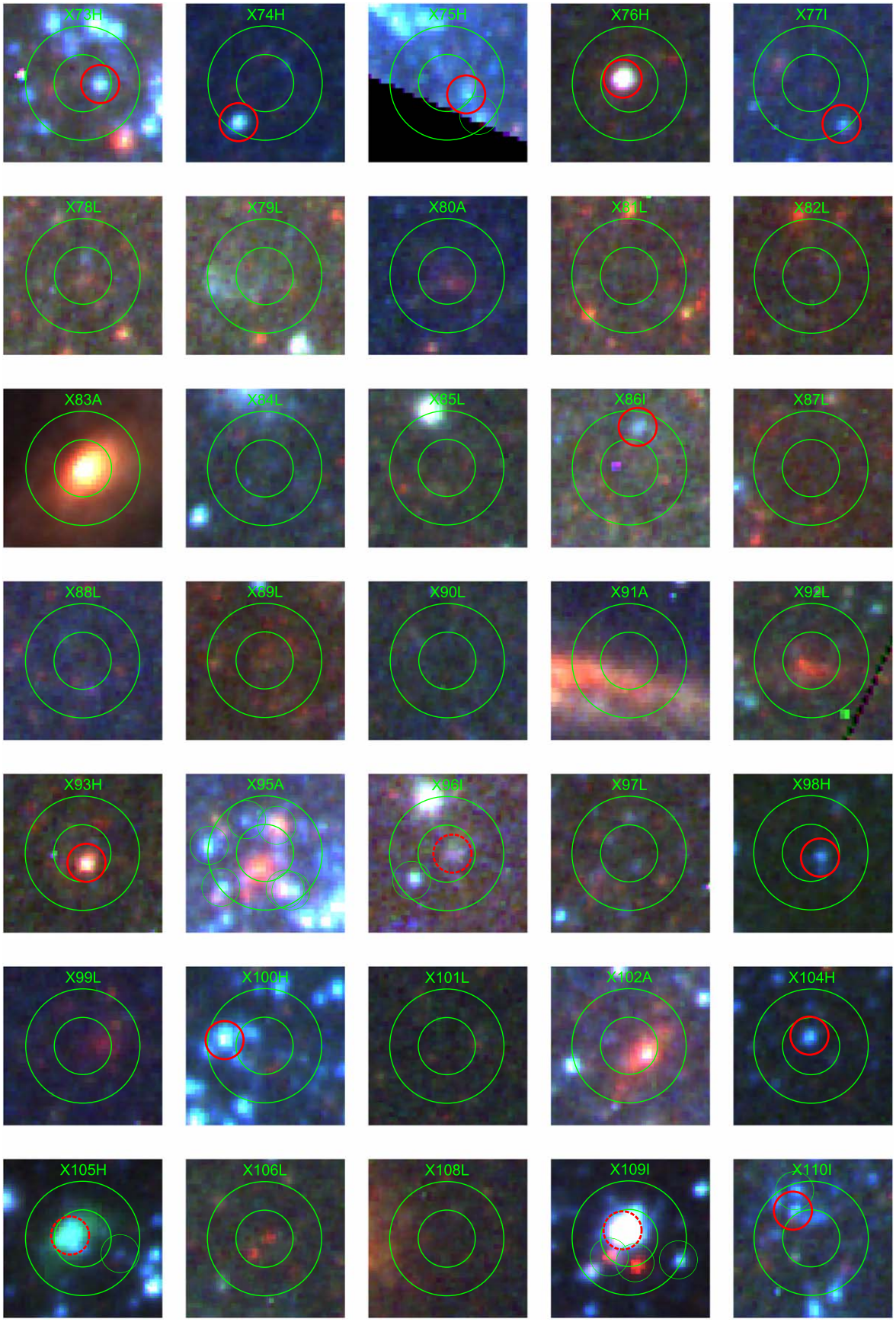

Figure 2. (Continued.)

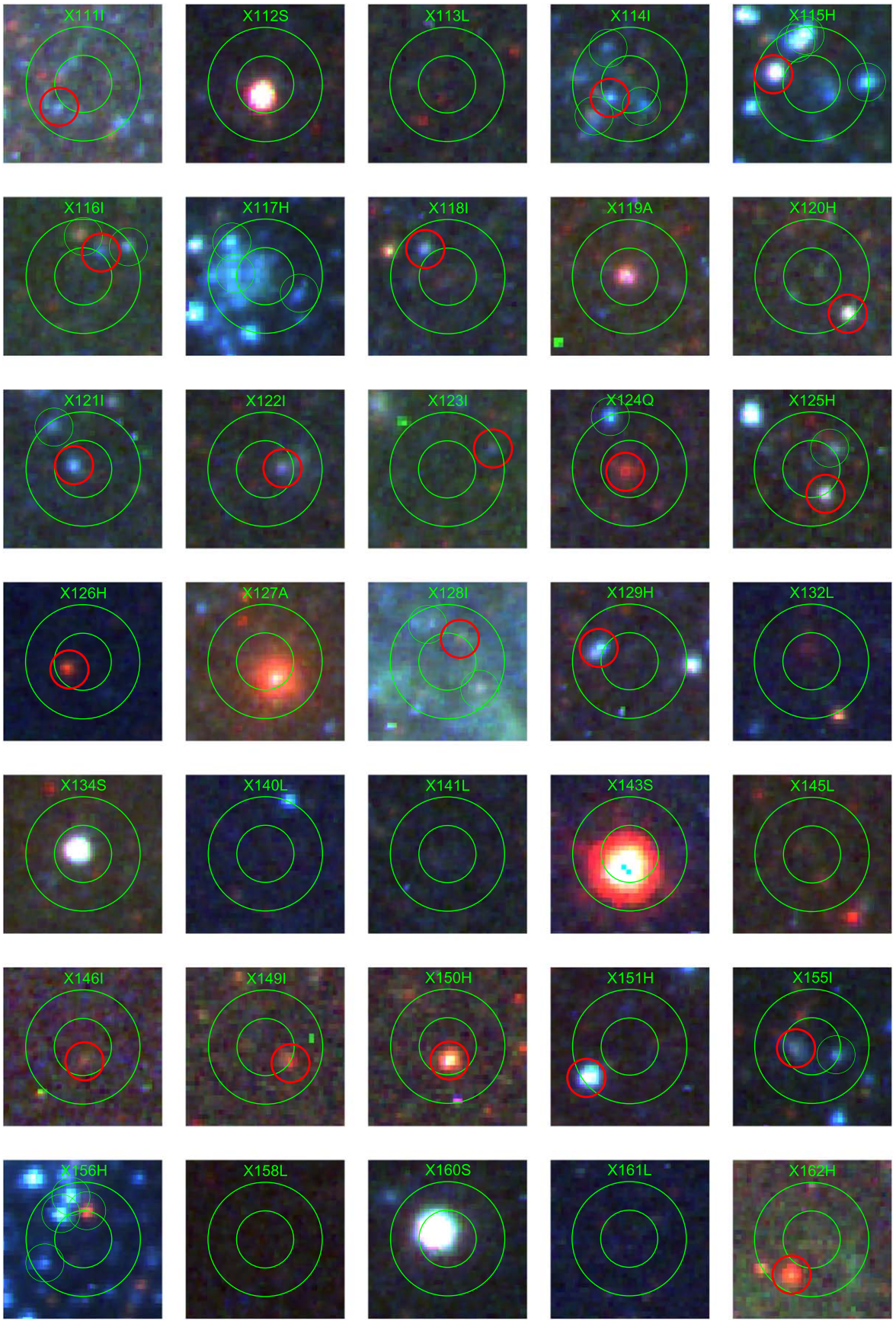

Figure 2. (Continued.)

Table 2
Results for X-Ray Luminosity Function Fits

Source Population	# Sources (This Work)	# Sources (Mineo+12)	PL Index (α) Flag = 1 + 2 + 3	PL Index (α) Flag = 1 + 2	PL Index (α) Flag = 1
All XRBs	124	...	-1.85 ± 0.07	...	...
HMXBs	44	96	-1.64 ± 0.08	-1.62 ± 0.07	-1.56 ± 0.09
IMXBs	33	...	-1.98 ± 0.13	-2.00 ± 0.15	-2.00 ± 0.18
LMXBs	47	24	-2.00 ± 0.11	-2.00 ± 0.11	-1.95 ± 0.17
CXBs	10	43	...	...	...

Note. The results are all from fitting a single power law, $dN/dL_X \propto L^{\alpha}$, to the observed distributions. The XRB distributions are well described by a power law and do not show statistically significant evidence for a downturn at the bright end.

source. From this, we find that most sources that we have classified as an HMXB are unlikely to change, since these tend to be in crowded, star-forming regions with a number of other bright stars nearby. Depending on the exact shape of the uncertainty contours, it is possible that ~10 sources classified as LMXBs might change to HMXBs, since they have a detectable star somewhere between 0.″6 and 1.″0 of the given X-ray position. In Section 5 we check the impact that a potential change in the classifications of these sources from LMXBs to HMXBs would have on the results of our XLFs, and find that it is within the uncertainties of the fitting results; therefore, we do not believe that our simplified treatment of the positional uncertainties has a significant impact on our results.

3.2. Classification Based on Parent Cluster Age

We find 10 (~10%) of the X-ray sources in M101 have an optical counterpart that is a compact stellar cluster rather than an individual donor star. Aperture photometry for the clusters was performed in the same way as for the donor stars, but with a size-dependent aperture correction to account for the fact that clusters are broader than the PSF. The aperture corrections follow the methodology described in Cook et al. (2019).

At the distance of M101, the stars within clusters are crowded too close together to allow unique identification of the donor star. However, it is possible to use the age of the cluster to classify the nature of the binary. The most massive stars in a cluster are the most dynamically active and therefore the most likely to form binaries. The hydrogen-burning lifetime of an 8 $M_{\odot}$ star is only a few tens of Myr, and longer than ~400 Myr for stars with masses $\lesssim$3 $M_{\odot}$ (for solar metallicity). This means that clusters with ages younger than a few tens of Myr likely host HMXBs, those with ages between this and a few hundred Myr likely form IMXBs, and clusters older than 400 Myr host LMXBs.

In Figure 4, we compare the measured $B - V$ and $V - I$ colors (with no correction for foreground extinction) of the clusters with predictions from the solar metallicity stellar evolutionary models of Bruzual & Charlot (2003). This figure shows that, over time, the integrated colors of clusters become redder. We estimate the age of each cluster by finding the closest model to its measured colors. A single cluster, X2, has colors similar to those of ancient globular clusters in the Milky Way. This X-ray source must be an LMXB, since the only potential donor stars in ancient globular clusters have masses $\lesssim$1 $M_{\odot}$. There are several clusters (X21, X43, X54, X62, X96, and X109) which have colors that suggest they are a few hundred Myr, and two host clusters (X105 and X109) that have ages younger than a few tens of Myr; the colors of X105 are to the left of the evolutionary model predictions, because this parent cluster is very young and has Hα line emission, as ultraviolet photons from massive, young stars ionize the remaining natal gas. The most massive stars in a cluster are the most dynamically active and therefore the most likely to form binaries (e.g., Garofali et al. 2012), so clusters with ages younger than a few tens of Myr likely contain HMXBs, and those with ages of a few hundred Myr likely form IMXBs (since they no longer contain stars as massive as 8 $M_{\odot}$.

The cluster age estimates and resulting XRB classification are listed in Table 1. Our final catalog contains 44 HMXBs, 33 IMXBs, 47 LMXBs, 10 background galaxies/quasars, and six foreground stars. The total X-ray luminosity of all XRBs in M101 is $L_X \approx 1.5 \times 10^{39}$ erg s^{-1}. We find that all sources classified as an HMXB (with flags of 1, 2 or 3) have a summed luminosity of $L_X = 8.9 \times 10^{38}$ erg s^{-1}, or approximately 60% of the total, with LMXB+IMXB contributing approximately 40%.

3.3. Assessing the Frequency of Misclassifications

Here, we describe the potential ways in which our X-ray sources may be misclassified, and assess the impact on our results.

1. The hard X-ray emission from a background AGN/quasar may be detected through the disk of M101 in regions that are optically thick (and hence no optical counterpart is detected), leading a CXB source to be misclassified as an LMXB.

   We believe that this type of misclassification is likely to be the most common in our catalog. Approximately 1000 sources deg^{-2} were detected in the *Chandra* Deep Field over the energy range of 2–7 keV down to similar flux levels as used here (Luo 2017). If we scale this number to the area covered by our survey, we expect $1000 \times \frac{106}{3600}$ sq deg ≈30 total background galaxies; in the optical, background galaxies can appear to be diffuse (ellipticals and spirals) or point-like (quasars).
2. A detected red point source (beyond the central ≈90″) could potentially be misclassified as the red giant donor star to an HMXB, when instead it is a distant quasar (the reverse misclassification has a far lower probability since the density of red supergiants in M101 is far higher than that of background quasars in our field of view).

   Distant quasars are more difficult to identify than AGNs in *HST* images because they appear as unresolved red point sources, and have properties that partially overlap with those expected of red supergiant stars in M101, potentially leading to some misclassifications. However, we believe that this is not a significant issue for our data set, because the space density of quasars on the sky is quite low.

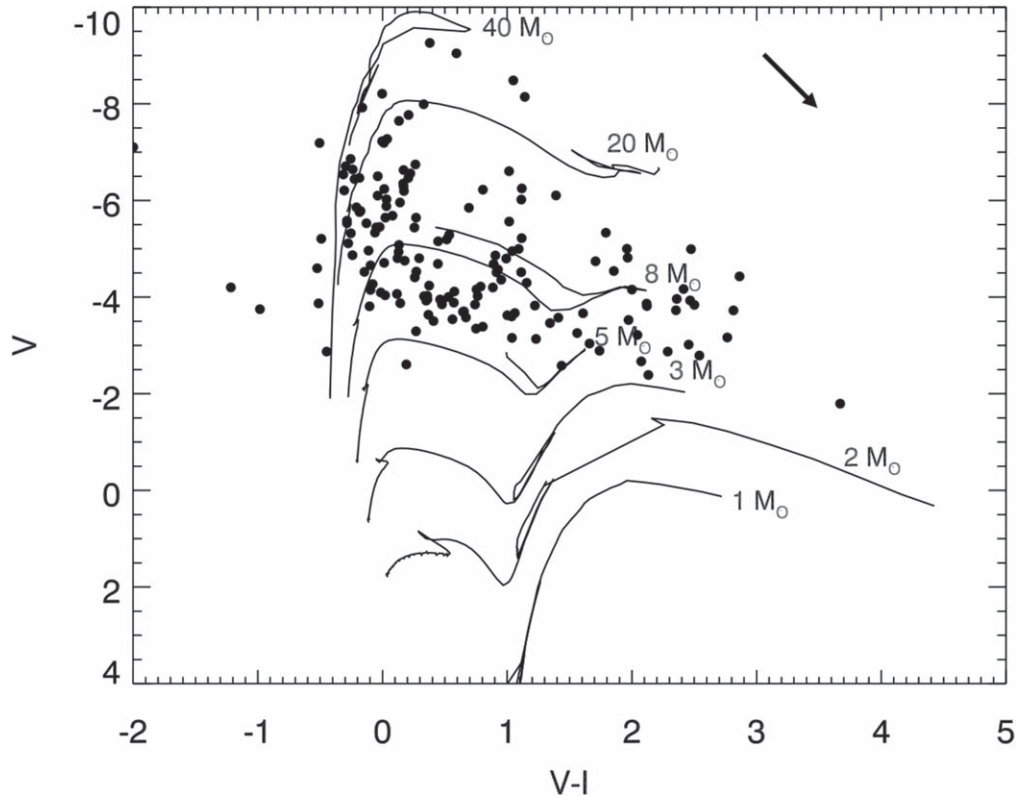

Figure 3. $V - I$ vs. V color–magnitude diagram of potential donor stars to X-ray binaries in M101 (circles)compared with predicted evolutionary tracks for stars of different masses, as labeled. The theoretical tracks are for solar metallicity from the Padova group.

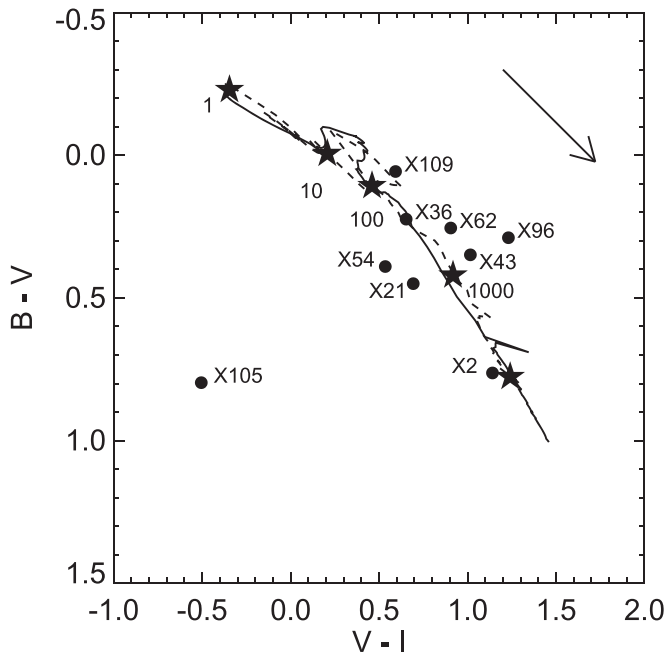

Figure 4. Measured $B - V$ and $V - I$ colors of X-ray binary host clusters in M101 (circles) compared with predictions for the color evolution of clusters from the Bruzual & Charlot (2003) models. The solid line shows predictions for solar metallicity and the dashed line for one-third solar metallicity. The stars show the predicted locations of clusters at the marked ages. We also represent an extinction of $A_V = 1$ with an arrow.

The optical colors and magnitudes of X-ray-selected quasars in the COSMOS field (Scoville et al. 2007; Brusa et al. 2009) overlap with those of the red supergiant stars in M101 shown in Figure 3. Between 50 and 100 of these are expected per square degree down to the X-ray completeness limit of our catalog, or 2–3 quasars in the field of view covered by our *HST* pointings. We have classified one X-ray source as a quasar, implying that we may have misclassified just one or two others.

3. A massive donor star in an XRB may appear less luminous (and hence less massive) due to extinction, leading an HMXB to be misclassified as an IMXB.

   In Section 3.1, we visually examined the region around each IMXB, and did not find evidence of dark patches or filaments, which are a clear signature of dust. For this reason, we expect a very low level of IMXBs misclassified as HMXBs due to extinction. From Figure 3, we see that a typical IMXB has a measured V-band magnitude that is $\approx$1 mag fainter than predicted by the 8 $M_\odot$ isochrone, which implies that these sources would need to have $E_{(B-V)} \approx 0.3$ (for a Galactic-like extinction curve with $R_V = 3.1$), a fairly significant level of extinction. This level of extinction is typical near very young ($\lesssim$3–4 Myr) stellar clusters in star-forming galaxies (e.g., Chandar et al. 2010; Whitmore et al. 2020), and is visually obvious in the color images. For these reasons, we expect very few of the sources identified as IMXBs to be misclassified HMXBs.
4. A source classified as an HMXB or IMXB based on seeing a candidate donor may actually have an "invisible" low-mass donor instead.

   While bright, massive stars and young stellar clusters tend to clump together but faint, older stars and clusters are distributed much more uniformly (Chandar et al. 2017), some regions can have high rates of star formation *and* high stellar mass. In such regions, there is a reasonable

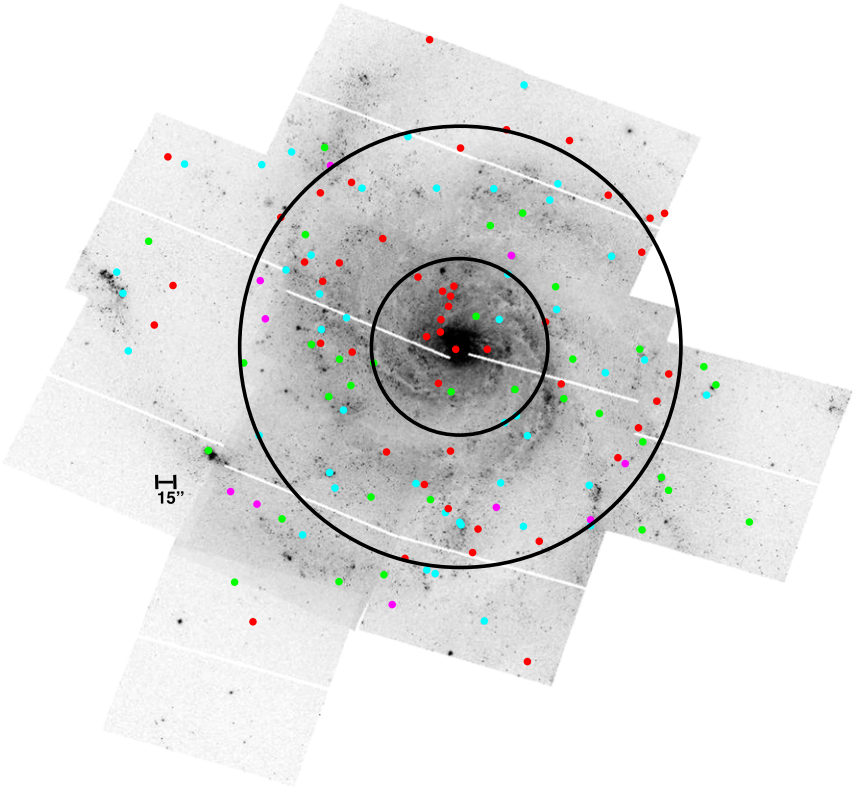

Figure 5. Source-by-source classifications of HMXBs (blue), IMXBs (green), and LMXBs (red) shown on a mosaic image of M101, taken with the *HST*. The magenta points show background AGNs. The inner black circle represents the "bulge" region defined by Mineo+12 at 90″, and the outer black circle represents the D_{25} optical radius, located at 225″. See the text for details.

probability that an LMXB might be classified as an HMXB or IMXB. We assess the prevalence of this type of misclassification in Section 4.4, where we compare our source-by-source classifications with the sSFR (SFR/M_*) maps of M101 created by Lehmer et al. (2019).

4. Spatial Distributions of X-Ray Sources

4.1. Contributions of X-Ray Sources at Different Radii

Mineo+12 used the spatial locations of X-ray sources in M101 to classify them as likely HMXBs, LMXBs, or CXBs. They assumed that X-ray sources within the "bulge" region (i.e., 2 bulge effective radii, 90″) shown as the smaller black circle in Figure 5 were all LMXBs, and those beyond the outer circle (located at 225″) were dominated by background sources, and excluded both from their analysis. The location of the outer circle was selected to minimize contamination from background sources in their analysis, and was determined by Mineo +12 as follows. They compared the cumulative and differential radial profiles of detected X-ray sources, with the (full X-ray band) log N–log S CXB distribution found by Georgakakis et al. (2008), to estimate the radius where the contribution of the CXB reaches 30% of the detected, compact X-ray sources. Based on their calculations, the contamination level from the CXB should reach ≈30% at a radius of ∼225″, and increase beyond it.

In the *HST* mosaic image of M101 presented in Figure 5, we show the locations of HMXBs (blue) and LMXBs (red) in M101, candidate IMXBs (green), and AGNs (pink), based on our source-by-source classification. From this figure, we find that the central portion of M101 is indeed dominated by LMXBs (red circles), but that there are some (seven out of 18 total or ∼40%) HMXBs or IMXBs. LMXBs tend to be closer to the center of M101, with an average distance of 1.6 kpc, compared with 2.1 kpc for HMXBs+IMXBs.

The annular region between the two black circles also contains a mix of LMXBs and HMXBs, now with a few background galaxies thrown in. Out of 74 total X-ray sources in this "disk" region, six are background AGNs (8%), 25 appear to be LMXBs (34%), 27 HMXBs (36%), and 16 have donor stars which have estimated masses just below 8 $M_\odot$ (22%).

Finally, we consider the region of M101 beyond the "disk" radius, where background sources are expected to increasingly dominate (Mineo+12). We find that XRBs associated with M101 are still the main X-ray source population in this region. Out of the 40 X-ray sources beyond the 220″ radius but still covered by the *HST* footprint, 11 (∼27%) are LMXBs, 13 (∼33%) are HMXBs, 13 (∼33%) are candidate IMXBs, and only four (∼10%) are background sources.

4.2. Spatial Distribution of LMXBs

One of the more interesting results from our source-by-source classification is that LMXBs are found throughout M101 and not just in the central bulge region. While HMXBs appear to lie mostly along spiral arms, the LMXBs appear to be belong to more of an an inter-arm population. Their spatial distribution suggests that there may be two distinct populations of LMXBs in M101: one associated with the bulge (the centrally concentrated red points in Figure 5), and another associated with the old stellar disk (the more dispersed red points throughout the image, including beyond the D_{25} radius).

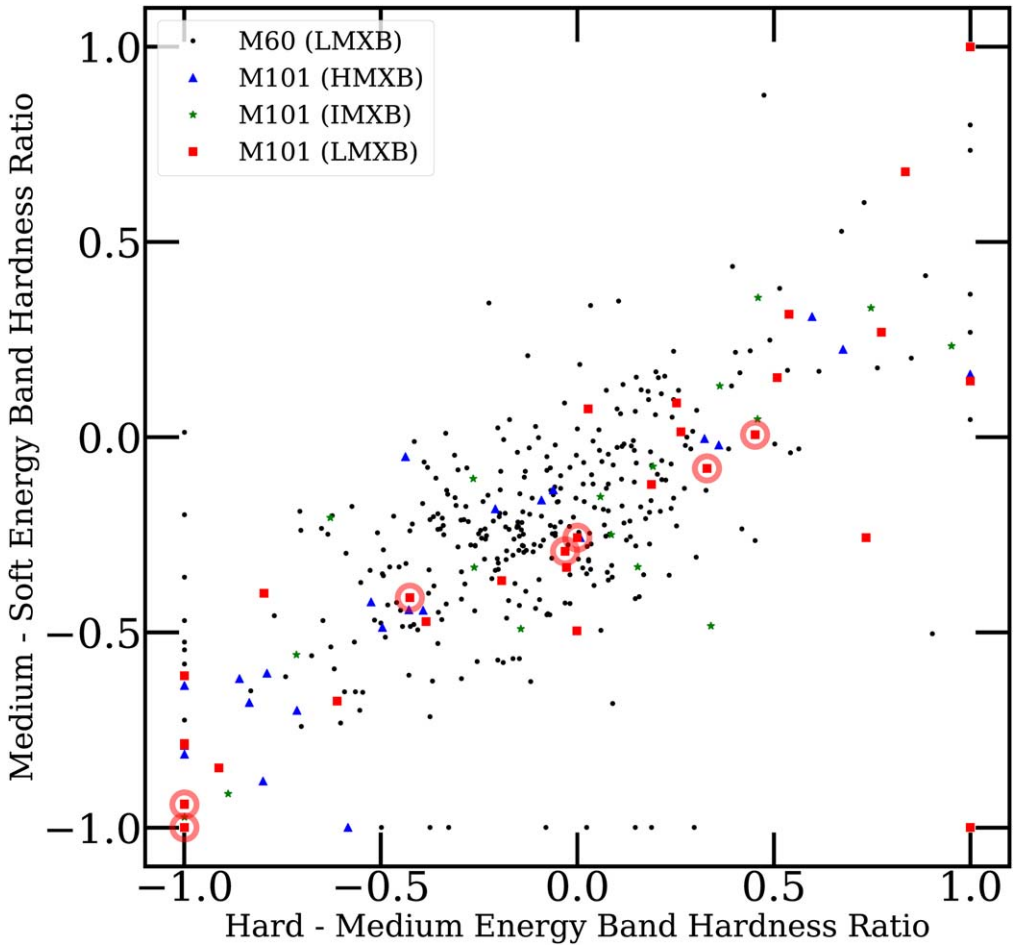

Figure 6. Comparison of X-ray colors for LMXB (red), IMXB (green), and HMXB (blue) in M101 with the LMXB population from the early-type galaxy M60 (small black circles). The X-ray colors of LMXBs in M101 that fall within the bulge region (circled) mostly have colors that overlap with those of LMXBs in M60, and likely are a true ancient population.

M101 is known to have formed a population of older star clusters in the disk (e.g., Barmby et al. 2006; Simanton et al. 2015), so perhaps it is not too surprising that a population of disk LMXBs has formed in this galaxy as well.

We compared X-ray colors (medium–soft versus hard–medium bands) of XRBs in M101 with those of LMXBs in the elliptical galaxy M60 (downloaded from the CSC), and show the results in Figure 6. The LMXBs in M60 show a fairly large spread in this color–color diagram. The HMXBs in M101 (blue) have X-ray colors that are somewhat distinct from the LMXBs in M60 (black dots), while the colors of the LMXBs in M101 (red) have somewhat better overlap with their counterparts in M60. We circle the LMXBs found in the bulge region, and find that the majority of them better overlap the LMXBs in M60. This may indicate that LMXBs associated with the bulge of M101 represent a true, old population like those in M60, whereas those in the disk are a distinct, somewhat younger population.

The presence of an old LMXB population in the disk of M101 suggests that the scaling relations developed for LMXBs in early-type galaxies may not apply to star-forming galaxies.

4.3. The Cosmic X-Ray Background near M101

Mineo+12 calculated that X-ray-emitting background galaxies should account for ≈30% of the total source population within the 225″ radius (outer circle shown in Figure 5), based on the background log N–log S relation determined by Georgakakis et al. (2008). Lehmer et al. (2019) gave a similar estimate based on the relationship found by Kim et al. (2007). This implies that there should be ≈25 AGNs and quasars within the 225″ radius, since 83 X-ray sources are detected in this region, and $83 \times 0.3 \approx 25$. Presumably, the fraction of background sources will continue to rise beyond this radius, since the number of XRBs associated with M101 is expected to drop along with the stellar luminosity.

We have found that 10 X-ray sources within the *HST* footprint are background AGNs or quasars, based on optical morphology, with six or $6/83 \approx 7\%$ located within the 225″ "disk" radius. This is only $\sim 1/5$ of the expected number. While it is possible that we may have misclassified a few background quasars as HMXBs, in Section 3.3 we suggested that this is likely to affect only a handful of objects. It is more likely that we detect X-ray emission from a background galaxy but do not detect it in the optical, either because the host galaxy is too faint or due to extinction from the disk of M101. In fact, most spiral disks are fairly opaque in their centers, based on counts of background galaxies (e.g., Holwerda et al. 2005, 2007). If we consider the entire *HST* field of view, we find 10 out of the expected ≈30 background sources, or $\sim 1/3$. Interestingly, a recent study of optical counterparts to X-ray sources in M31 also found significantly fewer background galaxies than expected (Williams et al. 2018). It seems likely

that if we are missing background galaxies, it is due to their intrinsic faintness rather than due to extinction from M101. The lower fraction of CXB sources that we detect directly compared with the number expected is either due to missing faint background galaxies in the optical images, or due to cosmic variance, since our observations cover such a small area of the sky.

4.4. Comparison with sSFR Maps

In spiral galaxies, it is expected that HMXBs will be preferentially found in areas of high recent star formation, while LMXBs should trace the stellar mass distribution. It is possible that some regions may have both a high SFR and high stellar mass. A map of the sSFR highlights regions dominated by recent star formation and those dominated by stellar mass.

Lehmer et al. (2019) created maps of sSFR for 38 nearby galaxies, including M101. They used *GALEX* far-ultraviolet plus *Spitzer* 24 μm images to create maps of SFR across their galaxy sample, and broadband optical and near-infrared images to create stellar mass maps. These were then used to create maps of sSFR, as shown for M101 in Figure 6. Here, the SFR dominates over stellar mass in the bright regions, and the stellar mass dominates over current star formation in the dark regions.

A comparison of the locations of our classified HMXBs (blue), IMXBs (greem), and LMXBs (red) with the sSFR map of Lehmer et al. (2019; Figure 7) reveals some interest results. We expect HMXBs to better correlate spatially with bright regions and LMXBs to preferentially fall in dark regions, although we do not expect a perfect correlation, since HMXBs can be expelled from their birthsites with high velocities (in these cases a high-mass donor star will be clearly detected). Overall, sources we classify as HMXBs are found either directly within or close to bright regions with high sSFRs; essentially no source that we classify as an HMXB is found in a dark region dominated by stellar mass. Sources that we classify as LMXBs are preferentially found in regions of low sSFR, including in the central portion of M101.

5. XLFs

In this section, we determine the shape of the XLF of XRBs in M101. We are particularly interested in establishing whether the XLFs of HMXBs and LMXBs have different shapes, and if there is evidence for a physical (rather than statistical) cutoff at the bright end of the distributions.

One advantage of our source-by-source classification over previous methods is that we do not need to make statistical corrections for X-ray-emitting foreground stars or background galaxies, or assumptions regarding the scaling of HMXBs with SFR or of LMXBs with stellar mass. Our approach however, is limited to galaxies out to $\sim$10 Mpc.

The black line in Figure 8 shows a histogram of the XLFs for all XRBs in M101 including HMXBs, IMXBs, and LMXBs (of all confidence classes), but excluding background AGNs/quasars and foreground stars. The number of sources increases steadily with decreasing luminosity down to approximately $L_X \approx 3 \times 10^{36}$ erg s^{-1} or log $L_X = 36.5$, where the distribution flattens. We assume that this flattening is caused by incompleteness in the X-ray point-source catalog, and set our completeness limit at this value. We note that our value is similar to the log $L_X = 36.3$ adopted by Lehmer et al. (2019) as their 90% completeness limit for sources in M101. Figure 6 also shows that the HMXB and LMXB distributions have clearly different shapes, with the HMXBs extending to brighter luminosities with a steeper slope than the LMXBs.

In order to quantify the shape of the luminosity functions, we consider two different distributions, a power law, $dN/dL \propto L^{\alpha}$ and a Schechter function, $dN/dL \propto L^{\alpha}e^{L/L*}$, where L_* is the characteristic luminosity where the distribution "turns down." The first method we use fits both a power law and Schechter function to the *binned* luminosity function (using equal size bins in log flux). This is the simplest way to visualize the data, and provides insight into the shape of the distribution, particularly the value of the power-law index, but is not particularly sensitive to weak cutoffs L_* (e.g., Mok et al. 2019). The second method fits a power law and a Schechter-like truncated power law to the *cumulative* luminosity distribution using the code MSPECFIT (Rosowlowsky 2005). This method returns the power-law index α, as well as a statistic, N_0, which assesses whether or not there is a statistically significant cutoff at the bright end of the distribution. We have found that fits to the cumulative distributions tend to return very stable results for the power-law index, so we will adopt these as the best fit values here. The third method performs a maximum likelihood fit of the Schechter function to the observed luminosities, and determines the best-fit values and 1, 2, and 3σ confidence intervals for α and L_* (Mok et al. 2019). This method has the advantage of not requiring binned data (which can hide weak features at the ends of a distribution) or cumulative distributions (where the data points are not fully independent of one another), and provides robust constraints on any cutoff L_*. Because we are interested in establishing whether or not the luminosity distributions have an actual physical downturn, we require any upper cutoff L_* to be detected at the greater than 3σ level.

The left set of panels in Figure 8 shows the results when each method is applied to the XLF of all XRBs in M101 (HMXBs + IMXBs + LMXBs). We find that the overall XLF appears to be well-described by a single power-law with $\alpha \approx -2$ in the left and middle panels. The bright end of the distribution in the bottom-left panel is consistent with randomly sampling from a pure power law—there is no statistically significant detection of a cutoff luminosity L_*, since the 2σ and 3σ contours remain open up to the highest tested luminosity (which is far brighter than any source in the sample).

In Figure 9 we also compare the XLFs for our HMXB (second column), IMXB (third column), and LMXB (last column) populations, and find notable differences. Here, we show the distributions when sources with all confidence flags (1 + 2 + 3) are included, but we have found that the results are similar when only confidence flags 1 + 2 or only 1 are used (albeit with larger uncertainties due to the smaller number of sources). The XLF for HMXBs extends to significantly higher fluxes and has a flatter distribution than those for LMXBs and IMXBs. The distributions for IMXBs and LMXBs appear to be similar to one another. Below, we present fits and quantitative results for these distributions.

For each distribution, i.e., all XRBs, HMXB, IMXB, and LMXB, the MSPECFIT broken power-law fit to the cumulative distribution returns values of N_0 that have a significance less than 3σ; therefore, we only show the best fit power laws to these distributions in the middle row of panels. The cumulative XLF for HMXBs is well fit by a single power law with $\alpha = -1.64 \pm 0.08$. The contours in the bottom panel of this

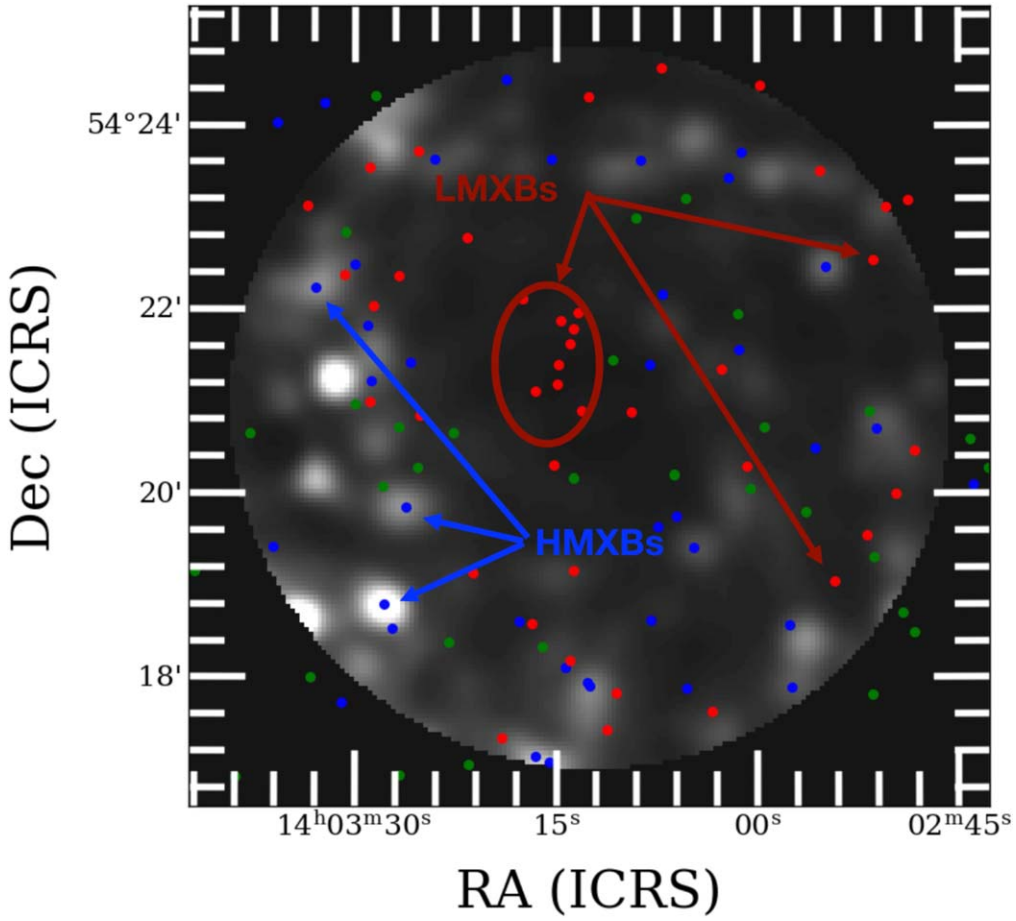

Figure 7. Locations of our classified X-ray binaries shown on the specific star formation rate image created by Lehmer et al. (2019), with the same color scheme as used in the previous image: HMXBs are shown in blue, IMXBs in green, and LMXBs in red. The HMXBs tend to fall in bright regions, i.e., in regions of the galaxy where the star formation rate (SFR) dominates over the stellar mass, as shown by the blue arrows. LMXBs, by contrast, tend to fall in dark regions, where the stellar mass dominates over the SFR.

column from the maximum likelihood fit confirm the MSPECFIT results, since the 1σ contour remains open all the way to the brightest tested luminosity, indicating that the bright end of the distribution is consistent with sampling statistics. The luminosity function for IMXBs in M101 is clearly steeper (top and middle panels in the third column), with $\alpha = -1.98 \pm 0.13$, again with no evidence at the $>3\sigma$ level for a downturn. The last column shows our results for LMXBs. These also appear to have power-law indices that are steeper than found for HMXBs, but not quite as steep as for IMXBs. We find a best fit of $\alpha = -2.00 \pm 0.11$. The best fit results from the cumulative fits for all XRBs, HMXBs, IMXBs, and LMXBs are compiled in Table 2. These are presented for confidence flag $= 1 + 2 + 3$, flag $= 1 + 2$, and flag $= 1$, which all give consistent results, within the uncertainties.

We repeat our fitting procedure to see how much the XLF results are affected if we assume larger positional uncertainties of $1''$ (as discussed in Section 3.1), where 10 sources currently classified as LMXBs would likely switch to HMXBs. In this case, we find very small differences (at the level of ≈0.03–0.05 for the power-law index α, well within the uncertainties) in the best fit values of α for the LMXB and HMXB luminosity functions, indicating that our simplified treatment of the uncertainties is not having a significant impact on our results.

Our main conclusions are that the XLF for HMXBs is shallower and extends to brighter luminosities than that for IMXBs and LMXBs, and that the bright end of all XLF distributions are consistent with sampling statistics from a pure power law, and do not require a truncation at the bright end.

6. Discussion

We use our classification of individual X-ray sources in M101 to separately study the populations of HMXBs and LMXBs in a massive spiral galaxy, and to compare with previous results.

6.1. HMXBs

HMXBs are known to be a good tracer of recent star formation in their host galaxy, but the scaling relations, for example the XLF normalized by the SFR, still have a fairly large dispersion between galaxies, which Mineo+12 suggest has a physical origin. All previous analyses (e.g., Grimm et al. 2003; Mineo +12) which have derived these scaling relations relied on the "spatial" method, assuming that HMXBs dominate the "disk" region, which starts at 2 effective bulge radii (1.′5 for M101), and extends out to a radius where the background contamination is expected to reach ≈30% based on the radial distribution of detected sources and the Georgakakis et al. (2008) distribution of

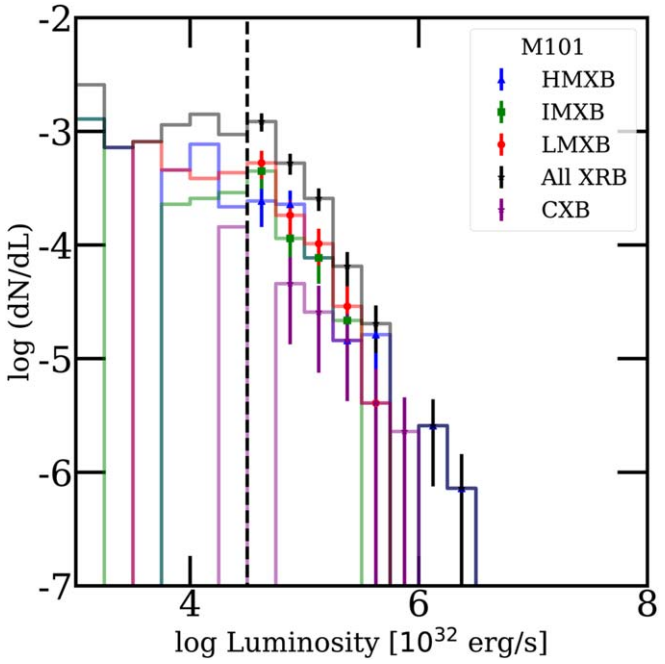

Figure 8. Binned XLF of all XRBs is shown as the solid black line. The dashed line shows our assumed completeness limit of log $L_X = 36.5$ erg s^{-1}. The luminosity functions for HMXB (blue), IMXB (green), and LMXB (red) classified in this work show differences in shape. The distributions plotted here include classifications with all confidence flags (1 + 2 + 3).

CXBs. They then make a statistical correction for background contamination.

In this work, we found (Section 4) that 44 of the 124 X-ray binaries that fall in the available *HST* footprint have a massive $M \gtrsim 8\ M_\odot$ donor, and are therefore HMXBs. It is possible that a small fraction of the 33 sources identified as IMXBs have a moderate amount of extinction (which we have not attempted to correct for here), which could increase the mass estimate of the donor star. However, we believe that this would only affect a handful of sources, since there are few obvious dust lanes or dark patches in the color images shown in Figure 2.

In the left panel of Figure 10, we compare cumulative XLFs of HMXBs from our work (solid curve) to that from Mineo+12 (dashed curve). Our distribution includes all 44 HMXBs, i.e., confidence flags of 1 + 2 + 3, while the Mineo+12 selection criteria result in 96 candidate HMXBs (between the two circles in Figure 5, which represent the "bulge" and D_{25} radii), and we statistically correct this distribution by their estimated 30% contamination fraction. It is important to recall that we would directly detect any massive $\gtrsim 8\ M_\odot$ donor star with moderate extinction in the optical images of M101, and therefore it is unlikely that we have underestimated the HMXB population within the field of view. In all cases, we only consider X-ray sources that fall within the *HST* footprint shown in Figure 1.

We find that the shapes of the distributions are similar between the two works, with best-fit power-law indices of $\alpha = -1.71 \pm 0.06$ (our catalog) and $\alpha = -1.65 \pm 0.03$ (Mineo+12 catalog), and no statistically significant evidence for a Schechter-like cutoff at the bright end. These results are also similar to the power-law index of $\alpha \approx -1.6$ found by Grimm et al. (2003) for HMXBs. The *normalizations* of the two distributions, however, are different, with the selection method used by Mineo+12 resulting in an XLF that has a higher normalization, by ≈0.25–0.3 dex, than our source-by-source classification procedure. This difference is slightly less than but similar to the dispersion of ≈0.4 dex in the normalization of the XLF/SFR relation between galaxies found by Mineo+12, and implies that there may be less scatter in the XLF/SFR relation between galaxies than previously reported; future work should revisit this relation using the classification methods described here.

Pairs of massive stars are the progenitors of HMXBs, and most massive stars form in stellar clusters. Although most XRBs are believed to be ejected from their parent clusters due to an asymmetry in the supernova explosion, we have found previously that at least some remain within their parent cluster, allowing for an estimate of the age of the system, and constraints on the donor mass, since the most massive remaining stars in a cluster are the most dynamically active. In Section 3.2, we found that 10 XRBs in M101 are coincident with a compact star cluster: one is in an ancient globular cluster, seven have parent clusters with ages of a few hundreds of Myr (likely IMXBs), and two have parent clusters with ages less than a few tens of Myr (likely HMXBs). The fraction of HMXBs that still reside in their parent clusters is significantly lower in M101 than found for the merging Antennae (Rangelov et al. 2012) and the dwarf starburst NGC 4449 (Rangelov et al. 2011).

6.2. LMXBs

Mineo+12 suggested that the well-known LMXB–galaxy mass scaling relation determined from *early-type* galaxies (Gilfanov 2004) does not appear to work in late-type galaxies, finding it significantly over-predicted the contribution of LMXBs in the latter, resulting in *negative* counts (see Section 7.3 in Mineo+12). Our direct method of classifying LMXBs (by the lack of a donor star down to ≈3 $M_\odot$) results in nearly twice as many LMXBs compared with Mineo+12 (47 versus 24, respectively).

However, Mineo+12 did not account for several effects. Lehmer et al. (2017) showed that the shape of the XLF in M51 appears to evolve with the age of the stellar population. A more recent, comprehensive analysis by Lehmer et al. (2019) included both ellipticals and spirals, and found that both types of galaxies can be described by a single global model: $\alpha_{\rm LMXB} \times L_X({\rm LMXB})/M_* + \beta_{\rm HMXB} \times L_X({\rm HMXB})/{\rm SFR}$, which has a different normalization for HMXBs than found by Mineo+12 (see Figure 8 in Lehmer et al. 2019). M101 is included in the Lehmer et al. (2019) sample, and appears to be well fit by this global model.

We note that the XLFs of LMXBs and of IMXBs are both steeper than those found for HMXBs in M101, similar to the results found by Lehmer et al. (2017) using a different approach for different age populations in M51. Previously, we studied the masses and densities of star clusters that host XRBs, and found tentative evidence that IMXBs and LMXBs are more likely to form in more massive and dense clusters, but that these parent cluster properties do not seem to have an impact on the formation of HMXBs (Johns-Mulia et al. 2019). We suggest that this may be due to different formation mechanisms, that very young HMXBs form from primordial pairs of

[4] We scale the luminosities published by Mineo+12 by 0.9125 to account for the difference in their assumed distance to M101 (6.7 ± 0.3 Mpc versus the 6.4 Mpc assumed here; $\frac{6.4^2}{6.7} = 0.9125$), resulting in a shift of ≈−0.04 in log L_X.

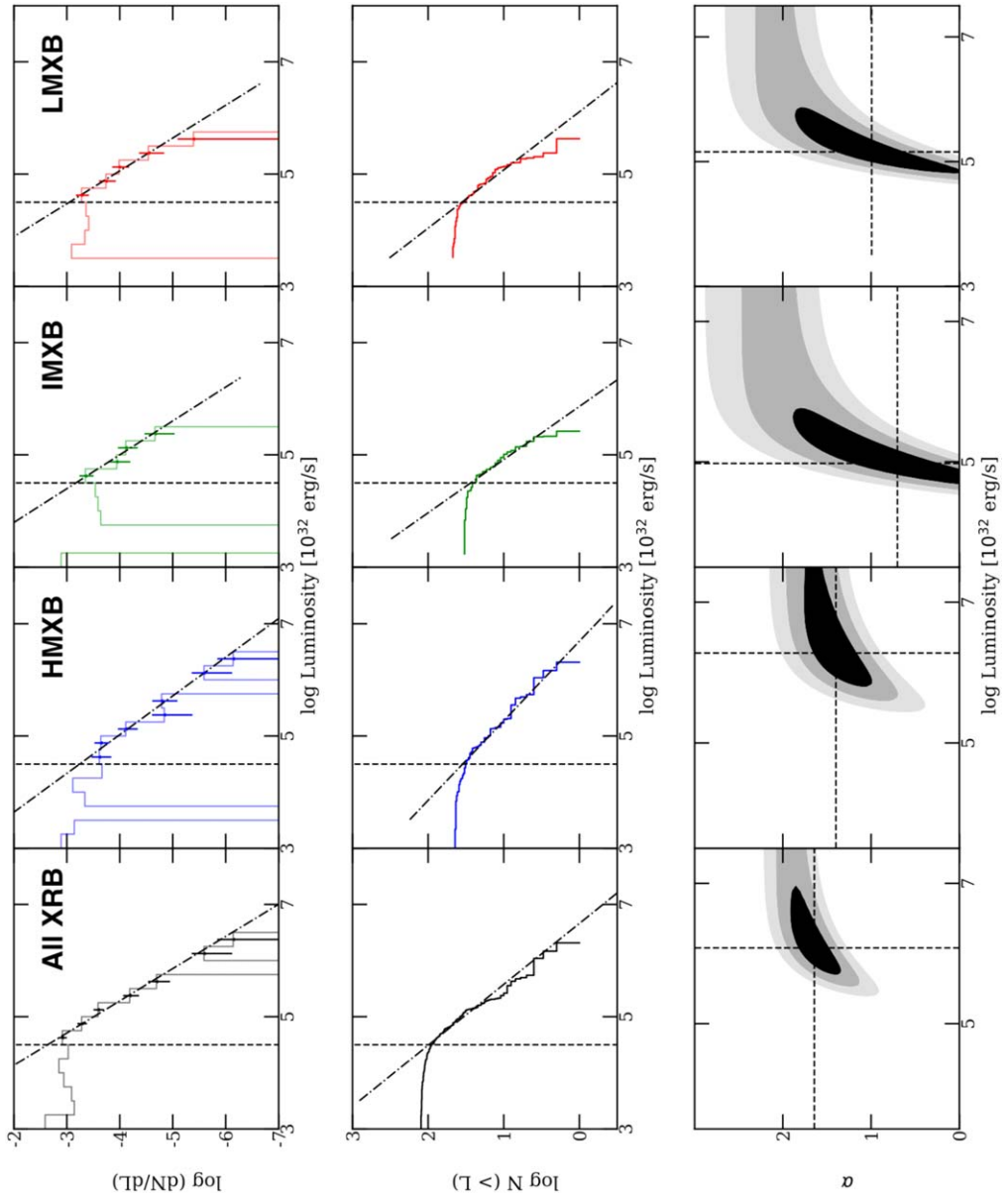

Figure 9. Results of fits to the XLFs of HMXBs (left panels), IMXBs (middle panels), and LMXBs (right panels). The top row shows the best-fit results to each distribution when equal size bins are used, the middle row shows the best power-law fit to the cumulative distributions, and the lower row shows the resulting 1, 2, and 3σ contours from fitting an underlying Schechter function the X-ray luminosities, as described in Section 5. The 3σ contours remain open to the right edge of each diagram, indicating that no Schechter-like cutoff is detected at this level for any of the luminosity functions.

massive stars while IMXBs and LMXBs are more likely to form through dynamical interactions within their parent clusters. Although tentative, the differences in the shapes of the XLFs of HMXBs versus IMXBs/LMXBs (shallower versus steeper) may also result from different formation mechanisms for the different types of XRBs.

In elliptical and lenticular galaxies, a significant fraction, between ≈20%–70% of LMXBs are found in ancient globular clusters (e.g., Angelini et al. 2001; Kundu et al. 2002, 2007; Sarazin et al. 2003; Jordan et al. 2004; Humphrey & Buote 2008). It is believed that dynamical interactions between the stars and compact objects in dense cluster cores are the primary formation mechanism for LMXBs in globular clusters (e.g., Jordan et al. 2007; Peacock et al. 2009). The XLFs of LMXBs in globular clusters and in the field are different at luminosities below $5 \times 10^{37}\,\mathrm{erg\,s^{-1}}$, which suggests that they are two distinct populations (Irwin 2005; Juett 2005; Maccarone et al. 2005; Kim et al. 2009). Two plausible mechanisms have been suggested for the formation of field LMXBs. One possibility is that they form in situ from evolved tight stellar binaries. However, because for a given stellar mass LMXBs are predominantly found in globular clusters, it is also possible that they form exclusively in globular clusters, but that the lighter ones are preferentially expelled through dynamical interactions within clusters into the field. In elliptical galaxies, LMXBs are more likely to be found in red, younger and/or more metal-rich clusters ($V - I > 1.1$) (e.g., Kundu et al. 2002; Jordan et al. 2004; Trudolyubov & Priedhorsky 2004; Kim et al. 2006). In M101, only a single X-ray source resides in an ancient star cluster, out of 47 LMXBs, or just ∼2%. This may be due to the fact that most of the ancient

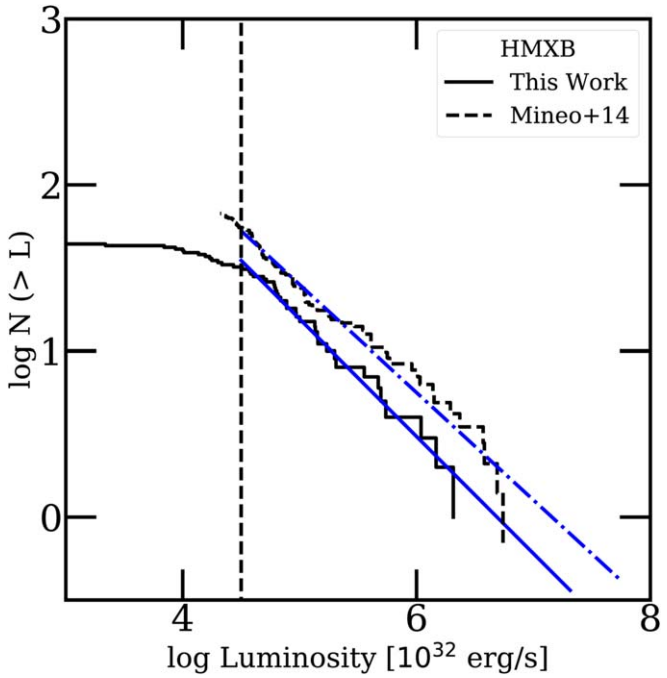

Figure 10. Comparison of XLFs for HMXBs between our work and that of Mineo+12. The luminosities in the latter have been adjusted to match the distance to M101 assumed here, and the distribution has been corrected for the 30% contamination fraction expected from background galaxies. See the text for details.

clusters in late-type spiral galaxies like M101 are metal-poor, and LMXBs appear to be produced more commonly in metal-rich globular clusters.

7. Conclusions

We have compared the locations of 140 X-ray point sources in the spiral galaxy M101 from version 2.0 of the *Chandra* Point Source catalog with optical images taken with the *HST*. We find a 1σ positional uncertainty of $\approx 0\farcs3$ for the X-ray source positions, similar to those found by previous works. Optical sources within 2σ of X-ray source positions were studied in order to determine the nature of the X-ray source: XRB in M101, background AGN or quasar, or foreground star. Each candidate XRB was further classified as high, intermediate or low mass based on the optical properties of the donor star.

1. We developed two methods to individually classify XRBs based on their optical properties, either based on the estimated mass or non-detection of a donor star, or the estimated age of the parent cluster. A total of 47 sources with no detected donor stars down to $\lesssim 3\ M_\odot$ are classified as LMXBs, and based on the estimated mass of the donor star we find 33 candidate IMXBs and 44 HMXBs. We also find 10 background AGN and five foreground stars.
2. Spatially, we find that HMXBs mostly follow the spiral arms, with some found within the bulge region ($\approx 90''$) and others out to the full extend observed by the *HST* footprint. LMXBs dominate the bulge region, but also appear throughout the disk, although appear to be more of an inter-arm population than HMXBs. No background galaxies/quasars are found within the bulge region, but are detected just beyond this radius.
3. We constructed the XLFs for HMXBs, IMXBs, and LMXBs, and found that all are well fit by a single power law, $dN/dL \propto L^{\alpha}$ including the bright end, which is consistent with the expectations from sampling statistics without requiring a physical cutoff. There were, however, differences in the power-law indices. We found the shallowest distribution for HMXBs, where $\alpha = -1.43 \pm 0.17$ for HMXBs, $\alpha = -2.05 \pm 0.46$ for IMXBs, and $\alpha = -1.71 \pm 0.26$ for LMXBs.
4. While the shape of the luminosity function for LMXBs in the spiral galaxy M101 appears to be similar to that found for LMXBs in the elliptical galaxy M60, the X-ray colors are different, as are the spatial distributions. Based on the spatial distribution, which appears to form an inter-arm population in the disk, we suggest that, in addition to truly ancient LMXBs, M101 also contains a contribution from the old stellar disk, with somewhat younger, more massive donors than in M60.
5. Using our new classification methods, we found around half the number of HMXBs as the previous Mineo+12 work (44 versus 96), with a few within the bulge region, near spiral arms throughout the "disk" region and beyond. While the shape of the XLF of HMXBs in our work is similar to that found previously, the *normalization* is different.
6. We identified 10 total individual background galaxies in our field of view from their optical morphologies and colors. This is around a third of the number expected from deep X-ray surveys, and likely due either to cosmic variance or some galaxies being too faint in the optical to be detected.

We have shown that classifying XRBs on a source-by-source basis and separating them from background galaxies and foreground stars is possible for galaxies within ≈ 7 Mpc, that have high resolution, deep, multi-band optical imaging taken with the *HST*. This approach allowed us to cleanly separate populations of HMXBs and LMXBs in star-forming galaxies, which resulted in similar shapes, but normalizations that differ from previous works.

In the future, a comparison of HMXBs in different star-forming galaxies, selected using the methods described, may reduce the scatter in the relationship between the XLFs of HMXBs and SFR. This method also enables the study of and comparison between populations of LMXBs in star-forming galaxies.

Facility: HST.

ORCID iDs

Rupali Chandar https://orcid.org/0000-0003-0085-4623
Angus Mok https://orcid.org/0000-0001-7413-7534

References

Angelini, L., Loewensteing, M., & Mushotsky, R. F. 2001, ApJL, 557, L35
Barmby, P., Kuntz, K., Huchra, J. P., et al. 2006, AJ, 132, 883
Bertelli, G., Bressan, A., Chiosi, C., et al. 1994, A&AS, 106, 275
Brusa, M., Comastro, A., Gilli, R., et al. 2009, ApJ, 693, 8
Bruzual, G., & Charlot, S. 2003, MNRAS, 344, 1000
Chandar, R., Whitmore, B. C., Fall, S. M., & Mulia, A. J. 2017, ApJ, 849, 128
Chandar, R., Whitmore, B. C., Kim, H., et al. 2010, ApJ, 719, 966
Cook, D. O., Lee, J. C., Adamo, A., et al. 2019, MNRAS, 484, 4897
Evans, I. N., Primini, F. A., Glotfelty, K. J., et al. 2010, ApJS, 189, 37

Garofali, K., Converse, J. M., Chandar, R., & Rangelov, B. 2012, ApJ, 755, 49
Georgakakis, A., Nandra, K., Laird, E. S., et al. 2008, MNRAS, 388, 1205
Gilfanov, M. 2004, MNRAS, 349, 146
Girardi, L., Dalcanton, J., Williams, B., et al. 2008, PASP, 120, 583
Grimm, M., Gilfanov, M., & Sunyaev, R. 2003, MNRAS, 339, 793
Holwerda, B., Draine, B., Gordon, K. D., et al. 2007, AJ, 134, 2226
Holwerda, B., Gonzalez, R. A., van der Kruit, P. C., et al. 2005, A&A, 444, 109
Humphrey, P. J., & Buote, D. A. 2008, ApJ, 689, 983
Irwin, J. A. 2005, ApJ, 631, 511
Johns-Mulia, P. N., Chandar, R., & Rangelov, B. 2019, ApJ, 871, 122
Jordan, A., Cote, P., Ferrarese, L., et al. 2004, ApJ, 613, 279
Jordan, A., Sivakoff, G. R., McLaughlin, D. E., et al. 2007, ApJL, 671, L117
Juett, A. M. 2005, ApJL, 621, L25
Kim, D.-W., Fabbiano, G., Brassington, N. J., et al. 2009, ApJ, 703, 829
Kim, E., Kim, D.-W., Fabbiano, G., et al. 2006, ApJ, 647, 276
Kim, M., Wilkes, B. J., Kim, D.-W., et al. 2007, ApJ, 659, 29
Kundu, A., Maccarone, T. J., & Zepf, S. 2002, ApJL, 574, L5
Kundu, A., Maccarone, T. J., & Zepf, S. 2007, ApJ, 662, 525
Lehmer, B. D., Berkeley, M., Zezas, A., et al. 2014, ApJ, 789, 52
Lehmer, B. D., Eufrasio, R. T., Markwardt, L., et al. 2017, ApJ, 851, 11
Lehmer, B. D., Eufrasio, R. T., Tzanavaris, P., et al. 2019, ApJS, 243, 3
Luo, B. 2017, ApJS, 228, 2
Maccarone, T. J., Kundu, A., Zepf, S. E., et al. 2005, MNRAS, 364, L61
Marigo, P., Girardi, L., Bressan, A., et al. 2008, A&A, 482, 883
Mineo, S., Gilfanov, M., & Sunyaev, R. 2012, MNRAS, 419, 2095
Mok, A., Chandar, R., & Fall, S. M. 2019, ApJ, 872, 93
Peacock, M. B., Maccarone, T. J., Waters, C. Z., et al. 2009, MNRAS, 392, L55
Peacock, M. B., & Zepf, S. E. 2016, ApJ, 818, 33
Rangelov, B., Chandar, R., Prestwich, A. H., & Whitmore, B. C. 2012, ApJ, 758, 99
Rangelov, B., Prestwich, A. H., & Chandar, R. 2011, ApJ, 741, 86
Rosowlowsky, E. 2005, PASP, 117, 1403
Sarazin, C., Kundu, A., Irwin, J. A., et al. 2003, ApJ, 595, 743
Schechter, P. 1976, ApJ, 203, 297
Scoville, N. Z., Aussel, H., Brusa, M., et al. 2007, ApJS, 172, 1
Shappee, B. J., & Stanek, K. Z. 2011, ApJ, 733, 124
Simanton, L. A., Chandar, R., & Whitmore, B. C. 2015, ApJ, 805, 160
Sirianni, M., Jee, M. J., Benitez, N., et al. 2005, PASP, 117, 1049
Trudolyubov, S., & Priedhorsky, W. 2004, ApJ, 616, 821
Whitmore, B. C., Chandar, R., Lee, J. C., et al. 2020, ApJ, 889, 154
Williams, B. F., Lazzarini, m., Plucinsky, P. P., et al. 2018, ApJS, 239, 13